W. SALMAN

FLAME AEROSOL SYNTHESIS AND CHARACTERIZATION OF PURE AND COPPER DOPED NANO-TITANIUM DIOXIDE

THE GRADUATE SCHOOL OF NATURAL AND APPLIED SCIENCES
OF
ATILIM UNIVERSITY

WAQED KHUDAYER SALMAN SALMAN

A MASTER OF SCIENCE THESIS
IN
THE DEPARTMENT OF CHEMICAL ENGINEERING AND APPLIED CHEMISRY

JULY 2020

ATILIM UNIVERSITY

FLAME AEROSOL SYNTHESIS AND CHARACTERIZATION OF PURE AND COPPER DOPED NANO-TITANIUM DIOXIDE

A THESIS SUBMITTED TO

THE GRADUATE SCHOOL OF NATURAL AND APPLIED SCIENCES

OF

ATILIM UNIVERSITY

BY

WAQED KHUDAYER SALMAN SALMAN

IN PARTIAL FULFILLMENT OF THE REQUIREMENTS

FOR

THE DEGREE OF MASTER OF SCIENCE

IN

THE DEPARTMENT OF CHEMICAL ENGINEERING AND APPLIED CHEMISTRY

JULY 2020

Approval of the Graduate School of Natural and Applied Sciences, Atılım University.

_____

Prof. Dr. Ali KARA
Director

I certify that this thesis satisfies all the requirements as a thesis for the degree of **Master of Science in Chemical Engineering and Applied Chemistry Atilim University.**

_____

Prof. Dr. Şeniz Özalp Yaman
Head of Department

This is to certify that we have read the thesis **FLAME AEROSOL SYNTHESIS AND CHARACTERIZATION OF PURE AND COPPER DOPED NANO-TITANIUM DIOXIDE** submitted by Waqed Khudayer Salman, Salman and that in our opinion it is fully adequate, in scope and quality, as a thesis for the degree of Master of Science.

_____

Assoc. Prof. Dr. Nesrin Ekinci Machin
Supervisor

Examining Committee Members:

Assoc. Prof. Dr. Nesrin Ekinci Machin
Chemical Engineering and Appl. Chem. Department, _____
Atilim University

Prof. Dr. Şeniz Özalp Yaman
Chemical Engineering and Appl. Chem. Department, _____
Atilim University

Assoc. Prof. Dr. Hakan Kayı
Chemical Engineering Department, _____
Ankara University

Date: *24.July.2020*

I hereby declare that all information in this document has been obtained and presented in accordance with academic rules and ethical conduct. I also declare that, as required by these rules and conduct, I have fully cited and referenced all materials and results that are not original to this work.

Name, Last Name: Waqed Khudayer Salman, Salman

Signature:

ABSTRACT

FLAME AEROSOL SYNTHESIS AND CHARACTERIZATION OF PURE AND COPPER DOPED NANO-TITANIUM DIOXIDE

Salman, Waqed Khudayer Salman
M.Sc., Department of Chemical Engineering and Applied Chemistry
Thesis Advisor: Assoc. Prof. Dr. Nesrin Ekinci Machin

July 2020, 74. Pages

Recently, applications of doped titanium dioxide nanoparticles are getting lot of attention from researchers. Especially nano-sized structures have found their way in the most promising research fields such as energy storage and production, carbon dioxide photo-reduction, pigments manufacturing, and water purification. Biggest interest is due to the enhanced characteristics of titania with better photocatalytic activity when it is doped.

Flame Spray Pyrolysis (FSP) is one of the manufacturing methods in the production of nano TiO_2, which is applied in this thesis. Operating parameters affect the morphology, crystallinity, optical properties, and the crystal phase of TiO_2 in FSP production. TiO_2, and 5 and 10 % copper doped TiO_2 (Cu/TiO_2) have been manufactured in a short residence time to avoid sintering. The products were characterized by X-ray diffraction (XRD), N_2 adsorption-desorption analysis (BET), scanning electron microscopy (SEM), transmission and high resolution electron microscopy (TEM/HRTEM) analysis, and ultra violet- visible- diffuse reflectance spectroscopy (UV-vis- DRS), in order to understand their characteristics such as crystallinity, morphology, particle size distribution, surface area, crystal phase content and optical properties. Characterization results of pure and Cu doped TiO_2 showed that, fine nanoparticles had been manufactured with a high surface area that increased with adding more copper. Rutile phase was found to be the dominating crystal phase. It has also been found that adding copper to TiO_2 increased the band

gap for the manufactured products in this work. The band gaps energy values for TiO_2, 5 % Cu/TiO_2 and 10 % Cu/TiO_2 were found as 3.59, 3.79 and 3.85 eV respectively.

Key words: Aerosol synthesis, Nanoparticles, Titanium dioxide, Copper doped titanium dioxide

ÖZ

SAF VE BAKIR KATKILI NANO-TİTANYUM DİOKSİTİN ALEV AEROSOL YÖNTEMİYLE SENTEZİ VE KARAKTERİZASYONU

Salman, Waqed Khudayer Salman
Yüksek Lisans, Kimya Mühendisliği ve Uygulamalı Kimya
Tez Yöneticisi: Doç. Dr. Nesrin Ekinci Machin

Temmuz 2020, 74. Sayfa

Son zamanlarda, katkılı titanyum dioksit nanopartiküllerinin uygulamaları araştırmacılardan büyük ilgi görmektedir. Özellikle enerji üretimi ve depolama, karbondioksit foto indirgeme, pigment üretimi ve su arıtma gibi araştırma alanlarında ümit verici sonuçlar elde edilmiştir. En büyük ilgi de, TiO_2'in katkılandığında daha iyi fotokatalitik özellik göstermesinden kaynaklanmaktadır.

Alev Sprey Piroliz (ASP), bu tezde de uygulanan, nano TiO_2 üretim yöntemlerinden biridir. ASP operasyon parametreleri üretimin sonunda TiO_2'nin morfolojisini, kristalliğini, optik özelliklerini ve kristal fazını etkiler. Bu tezde TiO_2 ve 5 ve % 10 bakır katkılı TiO_2 (Cu/TiO_2), sinterlemeyi önlemek için kısa bir reaktörde kalma süresinde üretilmiştir. Ürünler X-ışını kırınımı (XRD), N_2 adsorpsiyon-desorpsiyon analizi (BET), taramalı elektron mikroskobu (SEM), transmisyon ve yüksek çözünürlüklü elektron mikroskobu (TEM / HRTEM) analizi, ve ultra viole-görünür-difüz yansıtma (UV-vis-DRS) ile karakterize edilmiştir.. Kristallik, morfoloji, parçacık boyutu dağılımı, yüzey alanı, kristal faz içeriği ve optik özellikler gibi özellikleri aydınlatılmıştır. Saf ve Cu katkılı TiO_2'nin (Cu/TiO_2) karakterizasyon sonuçları, daha fazla bakır eklenmesiyle artan yüksek yüzey alanına sahip çok küçük tane boyutlarında nanopartiküllerin üretildiğini göstermiştir. Rutil fazın baskın kristal faz olduğu bulunmuştur. TiO_2'ye bakır ilavesinin uygulanan çalışma aralığında bant

aralığını artırdığı görülmüştür. TiO_2, 5 ve 10 % Cu/TiO_2 için bant aralığı enerji değerleri sırasıyla 3.59, 3.79 ve 3.85 eV olarak bulunmuştur.

Anahtar kelimeler: Aerosol sentezi, Nanopartiküller, Titanyum dioksit, Bakır katkılı titanyum dioksit

To My Mother Hanaa, My Father Khudayer,
My wife Huda and My Daughter Alaa,
My Brothers and My sister

ACKNOWLEDGMENTS

I wish to express my deep gratitude for the considerable support, cooperation and the guidance my supervisor Dr. Nesrin E. Machin has provided. She gave me the opportunity to work in a research team for designing, manufacturing and installation of Flame Spray Pyrolysis system and production of nanoparticles. It was a great experience full with learning, and it made me a better engineer and a new researcher.

Financial support provided by the Scientific and Technological Research Council of Turkey (TUBITAK, Grant No:117M165) is greatly appreciated.

I would like to thank my family, especially my mother Hanaa for her patience support and sacrifice to help me in building my future. Also I would like to thank my father Khudayer, who didn't live to see me young. I would like to thank my wife Huda who has stood by me for all the travails. She gave me support and help. She also supported the family during much of my graduate studies. Along with her, I want to acknowledge my daughter, Alaa. Good girl, and great sources of love and relief from scholarly endeavor. Special thanks for my brother Ahmed for being there for me whenever I need him.

Finally, I would like to thank my colleagues Mustafi Alhaleeb, Asli Onay, Bilge Bozkurt and Yagiz Turkyilmaz for their support in the Reaction Engineering and Combustion Research Laboratory directed by Dr. Machin.

TABLE OF CONTENTS

LIST OF TABLES

LIST OF FIGURES

CHAPTER 1

1. INTRODUCTION AND BASIC PRINCIPLES

1.1. Introduction

Among the many problems that the world is suffering from, two main issues are considered a tax of economic and population growth. The first one is the water scarcity, which doesn´t mean a lack of water supplies only, but also, it means the diminishing of freshwater resources. This water problem is regarded as a result of releasing high quantities of industrial water and sewage into freshwater resources like rivers and lakes [1]. The second problem is global warming, which is basically due to the ascending level of greenhouse gases from burning fossil fuel, removing forests and manufacturing activities. When the world realized the dangers of the issues mentioned above on the future of humanity, the governments, companies and research centers have been pushed to find solutions. These solutions must be cheap and environmentally friendly to replace the most widely used traditional technologies in energy, food production and manufacturing [2]. Using nanoparticle photocatalysts such as ZnO, TiO_2, CdS, CuO shows promising results in pollution prevention. They are subject to many investigations focusing on the production of clean energy and remediation of water and air. The innovations in modifying their morphology, structure, and performance are topics for many new types of researches.

Titanium dioxide or titania is a catalyst that has received the most attention in recent years. It has special characteristics that are in the interest of many researchers, such as the activity under illumination, stability, and availability. Titania nanoparticles and their modifications are topic for many investigations in energy production such as splitting water for hydrogen production [3, 4], environmental remediation (degrading pathogens and chemicals in water and air) [5, 6], production of some chemicals like methane or methanol through CO_2 reduction [7, 8] or methyl formate by selective oxidation of methanol [9]. It was also entered in investigation and manufacturing of sensors [10, 11], solar cells [12, 13] and batteries [14, 15].

However, titanium dioxide is not without any drawbacks. The high energy band gap limits its ability to use the visible light and makes it restricted under the Ultra Violet ray (UV), which is about 4-5% of the solar energy. Studies that worked on solving the problems of titania are focusing on modifying its characteristics by loading it with other materials like metals or nonmetals.

Copper has been getting an increased interest as a dopant for titanium dioxide. It is cheap and available, its oxides have a narrow band gap and an effective adsorption coefficient, but it gets photo-corrosion. Recent publications revealed the benefits of loading copper with titanium dioxide in narrowing the titanium dioxide's band gap and in prolonging the electron-hole recombination process.

This research aims to synthesize pure, and copper doped titanium dioxide nanoparticles using the flame spray pyrolysis (FSP) method and characterize the products. In the manufacturing process, a high gas to liquid flow ratio (GLFR, vast amount of oxygen dispersion and sheath gas compared to liquid) is used. Characterization of the products are done by using X-Ray diffraction, N_2 adsorption-desorption analysis (BET), scanning electron microscopy (SEM), transmission and high resolution transmission electron microscopy (TEM/HRTEM), and ultra violet-visible- Diffuse Reflectance spectroscopy (UV-vis-DRS) to find the effects of operating conditions on pure and copper doped titanium dioxide nanoparticle properties, such as morphology, crystallinity, particle size, surface area, optical properties and product purity. Band gap has particular importance because it directly affects the photocatalytic (optical) properties of TiO_2 and Cu doped TiO_2. Measuring the optical properties like band gap and absorbance are of great importance since they demonstrate the prepared photocatalyst's performance to work under illuminating conditions for various photocatalytic applications. Optical properties and phase transformation of pure and doped titanium dioxide produced using the FSP process under the effect of high GLFR have been rarely studied . In the previous studies where the high GLFR was used to create TiO_2 nanoparticle using the FSP process, the researchers were interested in controlling the particle size, morphology, and production rates. Hosein Torabmostaedi et al. [16] worked on a computer simulation for the synthesis of TiO_2 nanoparticles by FSP and through their study, they investigated the effect of different GLFR's in addition to other parameters. They

focused on the effects of these parameters on the properties of the flame, particle size, and production rate. Other properties concerning particle properties like phase transformation, crystal phase (anatase to rutile ratio), photocatalytic characteristics and morphology of the product have not been studied especially for doped TiO_2. Most of the studies for pure, metal, and nonmetal doped titanium dioxide using FSP process used nearly the same operation parameters as listed in Table 1.1.

Table 1.1 Manufacturing parameters of FSP process for some pure, metal and nonmetal doped TiO_2 previous studies.

Product	Liquid Precursor flowrate, ml/min	O_2 dispersion flowrate, l/min	Pressure drop, bar	CH_4 flowrate , l/min	O_2 flowrate, l/min	Sheath Gas flowrate, l/min	References
TiO_2 and Nb/TiO_2	5	5	1.5	1.5	3.2	5	[17]
TiO_2 and Fe/TiO_2	5	5	1.5	1.5	3.2	5	[18]
TiO_2 and Ce/TiO_2	5	5	2.5	1.5	3.2	-	[19]
Ag/TiO_2	5	5	1.5	1.5	3	5	[20]
Nb/TiO_2 and Cu/TiO_2	5	5	1.5	1.13	2.4	-	[21]
TiO_2 and Ce/TiO_2	5	4.5	1.5	1.5	3	5	[22]
TiO_2 and S/TiO_2	3	5	1.5	1	1	3	[23]
TiO_2 and N/TiO_2	3	5	1.5	1	1	3	[24]
TiO_2 and V, Cr, Fe, Co, Mn, Ni, Cu, Y, Ce, and Zr/TiO_2	3	5	1.5	1	1	3	[25]
V/TiO_2	2.5	4.5	1.2	1	2.4	5	[26]
Cu/TiO_2 and Cu-Pt/TiO_2	4	5	2	1	2	-	[27]
TiO_2 and Pt, Sn, and Al/TiO_2	5	5	1-1.5	1.5	3.2	5	[28]
Au-Pd/TiO_2	5	5	1.5	1.5	3	25	[29]
CuO/TiO_2	5	5	1.5	0.75	1.5	-	[30]

1.2. Literature Review

1.2.1 Characteristics of Semiconductors

The materials that have connectivity between the high conductive materials and the nonconductive materials (insulators) are called semiconductors. These materials are generally considered as semiconductor if they have band gap range from 1 to 4 eV. Insulators have more than 4 eV band gap, and for conductors, the valence and conduction bands may overlap, so they may not have a band gap [31, 32, 33]. Atomic interactions of semiconductors give them their properties. The probability of electron transporting from valance to conduction band increases with increasing temperature, or it depends on the amount of energy absorbed by the semiconductor [31].

1.2.2 Photocatalysis

The process accomplished by using a catalyst with an ability to be activated by illumination called photocatalysis [34]. Ideal catalysts for this job are the semiconductors. The reaction that takes place on the surface of the photocatalyst is called photoreaction. Photocatalyst (such as those listed in Table 1.2) has a vital function in the photocatalysis process.

Table 1.2 Band gap energies of some semiconductors.

Photocatalyst	Bandgap energy (eV)
ZnS	3.6
TiO_2 (anatase)	3.2
TiO_2 (rutile)	3.0
WO_3	2.8
SnO_2	3.6
Fe_2O_3	2.3
V_2O_5	2.8

Semiconductive metal oxides are typically regarded as photocatalysts because of their electronic structure. But semiconductors have some drawbacks that hinder their uses. Their properties must be studied and tested before using them in the targeted applications. For example, characteristics like toxicity, unstability and photo-corrosion is not allowed in water remediation, and also the larger band gap is not feasible economically as it is considered as energy consuming. Other characteristics like fast recombination, chemical and biological stability must be examined [35].

The mechanism of photocatalysis starts when a photocatalyst is exposed to an energetic light source (natural or artificial) under the presence of an oxidation agent like oxygen or air [34]. If the absorbed energy (photonic energy) is higher than the semiconductor's band gap energy (which is the difference between the conduction and valance band), an electron jump from the valance band (where it will leave a hole) to the conduction band. If the photon energy is lower than the bandgap ($h_v < \Delta E$), the energy dissipates in the form of heat. In the case of ($h_v > \Delta E$), both the transported electron in the conduction band and hole in the valence band are trapped at the reactive surface sites. The jumped electron (e^-) make a reduction reaction with a material that accepts the electron (A), meantime an oxidation reaction is done by the formed positive hole (h^+) in the valance band participation of an electron donor (D) as presented in Figure 1.1. The following equation represents the photoexcitation:

$$semiconductor + hv \rightarrow e^- + h^+$$

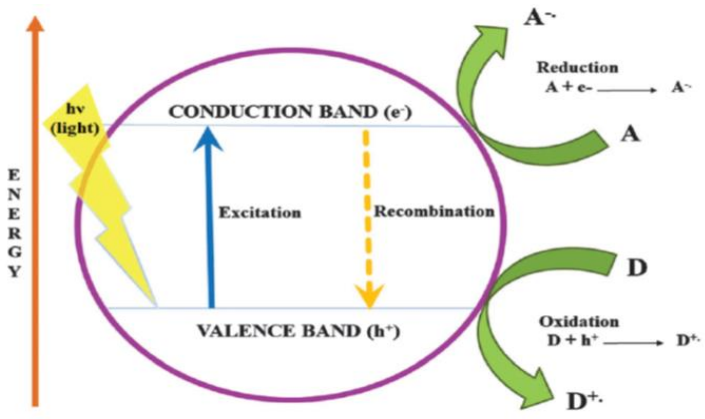

Figure 1.1 Basic mechanism of photocatalysis process [36].

1.2.3. Titanium Dioxide

TiO_2 is an n-type intrinsic semiconductor used broadly as a photocatalyst to induce on its surface series of reductive and oxidative reactions. Before starting to describe the characteristics of titania and modification processes that used to give it better properties, it is necessary to write a brief review about the setbacks of other semiconductors, and why titanium dioxide is the most favourable. An ideal semiconductor that is used as a photocatalyst must be photoactive, chemically and biologically stable, nontoxic for human and environment, and economical in terms of manufacturing and effectiveness when used in photocatalytic applications [37, 38]. ZnO has certain disadvantages, such as restriction in the use of visible light, which account for about 43% of the solar energy spectrum, wide bandgap (3.3 eV), Near-UV absorption of the spectral range, particle aggregation during the photocatalytic reaction and notable photo-corrosion that significantly limits the large-scale photocatalytic activity of ZnO [39]. Metal Sulphide semiconductors such as PbS and CdS are unstable as they undergo photo-corrosion under aqueous conditions and form toxic products [40]. A catalyst like SnO_2, its species is very unstable, the recombination of electrons and holes can occur quickly, and it needs external electrical alternative [41]. Fe_2O_3 also needs an external electrical charge to perform their hydrolysis reactions; it has the problem of corrosion and formation of short-lived ligand to metal charge transfer states [42]. WO_3 does not supply sufficient potential for O_2 reduction. Thus, WO_3 is not able to scavenge photogenerated electrons to reduce molecular O_2, which leads to the fast charge carrier recombination rate and therefore, depress the photonic efficiency [43]. Cupric oxide CuO_2 and cuprous oxide Cu_2O have low bandgaps 1.4 eV and 2.2 eV, respectively, which make them active under visible light, but they are not stable because of the occurrence of photo-corrosion.

Titanium dioxide is not an exception, as previously mentioned in the introduction, titanium dioxide has some disadvantages, but it has the lowest drawbacks among the other semiconductors. It is cheap, photo-stable, non-toxic, has good selectivity, has the capability to generate longer lived electrons and holes or the lowest recombination rate and it is chemically and biologically stable, in addition, it doesn't have the problem of photo-corrosion or the need for external electrical current for initiating the reactions on its surface. To solve the problem of the wide band gap and

the other disadvantages of titania, scientists have studied several paths to improve the properties of titanium dioxide using a wide range of metals and nonmetals.

1. Structure and Properties of TiO_2

Photocatalytic activity of TiO_2 relies on its surface and structural characteristics such as surface area, crystal composition, surface characteristics, band gap energy value, particle size distribution and surface hydroxyl density [44]. Titanium dioxide exhibits three polymorphs: Rutile, Anatase, and Brookite, depending on the method of manufacturing or formation (Figure 1.2).

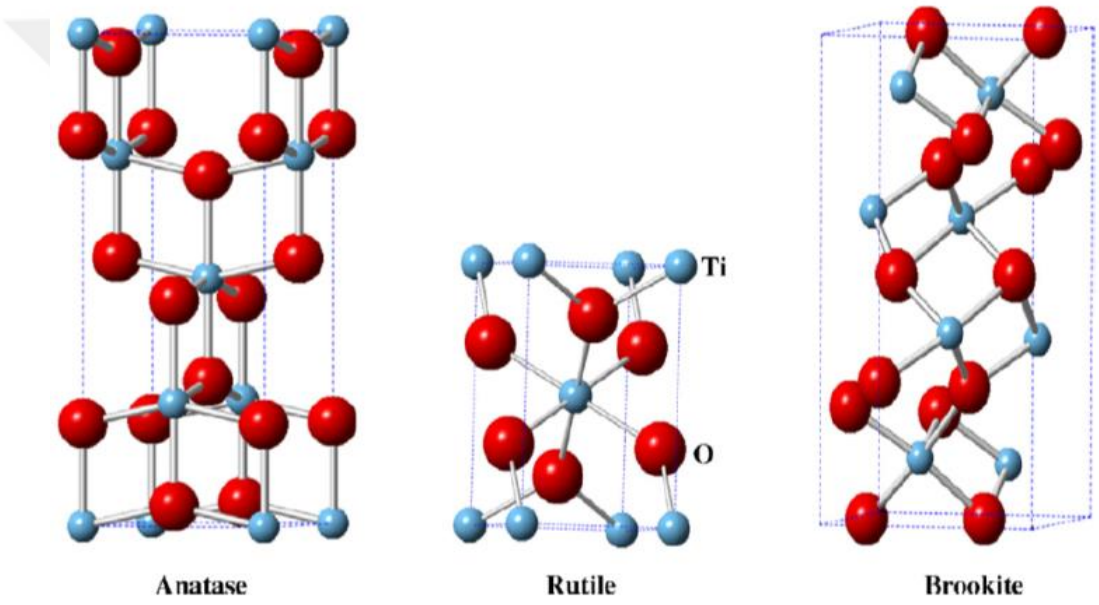

Figure 1.2 Crystal structures of Anatase, Rutile and Brookite TiO_2 [44].

Rutile is the stable phase, both Anatase and Brookite are metastable; the latter is difficult to synthesize, and so it is rarely studied [44]. Table 1.3 illustrates the properties of rutile and anatase phase of titania.

Table 1.3 Structural properties of crystalline structures of TiO_2 .

Properties	Crystalline forms	
	Anatase	Rutile
Crystalline structue	Tetragonal	Tetragonal
Lattice constants (nm)	a = b = 0.3733	a = b = 0.4584
	c = 0.9370	c = 0.2953
Bravais lattice	Simple,Body centred	Simple, body centred
Density (g/cm^3)	3.83	4.24
Melting point(℃)	580	1870
Boiling point(℃)	2927	-
Band gap (eV)	3.2	3.0
Refractive index	2.5688	2.9467
Standard heat capacity	55.52	55.60
Dielectric constant	55	110–117

Brookite TiO_2 belongs to the crystal group of orthorhombic. Its unit cell consists of eight TiO_2 formula units and is formed by TiO_6 octahedral edge-sharing. It is more complex, has a larger volume of cells and is also the least compact one of the three types, and is not often used for experimental research [45].

Anatase TiO_2 has a tetragonal structure. It is the metastable phase of titanium dioxide, it has a larger surface area and higher photocatalytic activity compared to rutile TiO_2 [46]. Consequently, it is the most widely used one. Nevertheless, it is not stable thermally. It transforms into the rutile phase when it exposed to high temperature; the rate of its transformation depends on the particle size. The nano-sized anatase particles have a phase transformation at temperatures between 500 and 600 ℃ [46]. The characteristic of phase transformation into rutile stifles the use of anatase phase in the applications that require high thermal stability such as ceramic materials. The new researches aim to improve the anatase performance under high thermal

conditions. These researches include adding new material to it, like metals or nonmetals, to make it more stable thermally. The investigations involve doping it with metals like Copper, Niobium, Iron, Platinium, and Aluminium. Besides, co-doping it with metals and nonmetals such as Nitrogen and Copper or metal-metal co-doping [47].

Rutile TiO_2 has also a tetragonal structure and contains six atoms per unit cell. Rutile is more stable chemically and thermally than anatase [48, 49]. It has a higher specific gravity and reflective index. The photocatalytic activity of the rutile is commonly reduced as compared with anatase even though it has a narrower band gap (3.0 eV) as compared with the band gap of anatase (3.2 eV), this is because it has lower negative reduction potentials of the conduction band electrons and a quicker recombination rate of electron-hole pairs [50]. The poor activity of rutile phase is attributed to (1) the size of its nanoparticles which is larger than that for the anatase phase, (2) the occurrence of a higher electron-hole recombination rate which makes the formed hydroxyl groups on its surface very limited and (3) due to limited electron lying at the conduction-band that lowers photocatalytic efficiency produced, so its applications were limited in pigments [50, 51]. Nevertheless, rutile titanium dioxide is not a useless phase; it is the most chemically and thermally stable phase of TiO_2. These properties in addition to the possibility of doping it with a wide range of materials were encouraging reasons for more studies aiming to extend its uses to more photocatalytic applications. Tryba et al. [52] prepared 80 % rutile phase copper doped titanium dioxide nanoparticles with lower bandgap energy (2.82-2.83 eV). It showed superior activity in degrading phenol. Inturi et al. [25] tested the photocatalytic activity of titanium dioxide against acetonitrile in a vapor phase, they compared P25 and FSP manufactured pure and doped titanium dioxide with 11 transition metal ions (V, Cr, Fe, Co, Mn, Mo, Ni, Cu, Y, Ce, and Zr). They found that Cr doped TiO_2 with the highest rutile content, 44 % among the other photocatalysts, showed a comparable photocatalytic activity. It exhibited a rate constant about 8–19 times higher than the rest of the other transition metal-doped catalysts with the highest anatase content. Xia et al. [53] synthesized a 100 % rutile phase of pure and copper doped titanium dioxide via a simple aqueous phase method at 85 ℃ . Six samples have been prepared from A-F with a Cu/Ti atom ratios as follow 0 %, 1 %, 2 %, 5 %, 10 % and % 20 they were used to degrade aqueous brilliant red X-3B solution at 7 pH reaction medium. The

samples showed a photocatalytic activity according to the following order sample C > sample D > sample E > sample F > sample B > sample D, from the best photoactivity to the worst. The results assert that the rutile phase activity could be enhanced by adding impurities to it, but the excessive amount of copper decreases the mineralization. Chen et al. [54] prepared pure rutile titanium dioxide nanorods under hydrothermal conditions under 220 ℃ , they prepared different samples by changing the time of hydrothermal treatment as (1, 5, 10, 15, 20, 24) hour, later the photocatalytic activity of the samples were tested with methylene blue (MB), they found that the rate of degradation increases with increasing the time of hydrothermal treatment. However, it decreases for the sample prepared hydrothermally for 24 hours, the results proved that with increasing the time of hydrothermal treatment the crystallinity increases as well, but with increasing the crystallinity the surface area also decreases, this is why a decrease in the photoactivity with the last sample has occurred.

It has been reported in some literature that mixing small amounts of rutile with anatase shows better photocatalytic activity than using pure anatase or rutile in liquid phase applications. This synergistic effect of the diphasic mixture is due to the forming wells of energy at the lower band gap of the rutile phase that works as an electron trap that prevents or delays the electron-hole recombination [55]. Ahmed et al. [55] reviewed several studies about the activity of some commercial TiO_2 samples which have different amounts of anatase/rutile ratios, like Degussa P25 Hombikat, UV100, PC500, PC 10, PC 50, Rhodia and Travancore Titanium Products (TTP), (their specifications and compositions listed in Table 1.4) in degrading of various herbicides and pesticides derivatives. They found that their efficiency is as follow: P25 > UV100 > PC500 > TTP. Poulios and Kositzi [56] studied the methomyl photocatalytic oxidation by P25, ZnO, and UV100. The reduction order of photocatalytic dissolved organic carbon (DOC) was reported to be: P25 > ZnO > UV100. Enríquez et al. [57] studied the degradation of 4-Chlorophenol and the results were : P25 > PC10 > PC50 > PC500 > Rhodia. The superior photoactivity of Degussa P25 has been ascribed to its crystalline composition (mixture Rutile and Anatase). It was postulated that the rutile's smaller band gap absorbs the photons and produces electron-hole pairs. Then the electron transfer occurs from the Rutile CB to electron traps in the Anatase phase. Thus it hinders the recombination process and let the hole to move to the surface of the particle to react [58].

Table 1.4 Specification and phase composition of some commercial TiO_2 samples.

Commercial Titania product	Specific surface area BET m^2/g	Crystallite size (nm)	Phase Composition	Reference
P25	50	22 Anatase 32 Rutile	20-30% Rutile	[59, 60]
P90	90	13 Anatase 23 Rutile	7.7-10% Rutile	[59, 60]
PC500	287	5-10	100% Anatase	[61]
UV100	250	5	100% Anatase	[61]
S5-300A	330	NA	100% Anatase	[6]
TTP	9.82	N/A	N/A	[61]
ST01	312	9	100% Anatase	[60]
PC 10	10	65-75	100% Anatase	[57]
PC 50	54	20-30	100% Anatase	[57]
Rhodia	150	N/A	100% Anatase	[57]
Tytanpol A11	11.4	37.3	100% anatase	[62]

2. Synthesis of Titanium Dioxide

The biggest challenge in the synthesis of titanium dioxide is improving its properties and manufacturing it with a safe, environmentally friendly and economical method. To enhance its properties, titanium dioxide has been manufactured in different shapes such as spheres [63], nanofibers [64], nanorods [65], nanotubes [66], nanosheets [67], and interconnected architectures [68]. The modifications on the structure of titanium dioxide give it some advantages in maximizing photocatalytic activities by enlarging the surface area. However, they don't give it the ability to work under the visible light range, which considered to be more feasible economically. So there is a need to modify its band gap by loweing it to give it this advantage.

There are many manufacturing methods for pure and modefied titanium dioxide like sol-gel [69], hydrothermal [70], flame synthesis [71, 72], hydrolysis [73], impregnation [74], microwave assist [75] and solvothermal [76]. Figure 1.3 illustrates some of the methods used for manufacturing of titania.

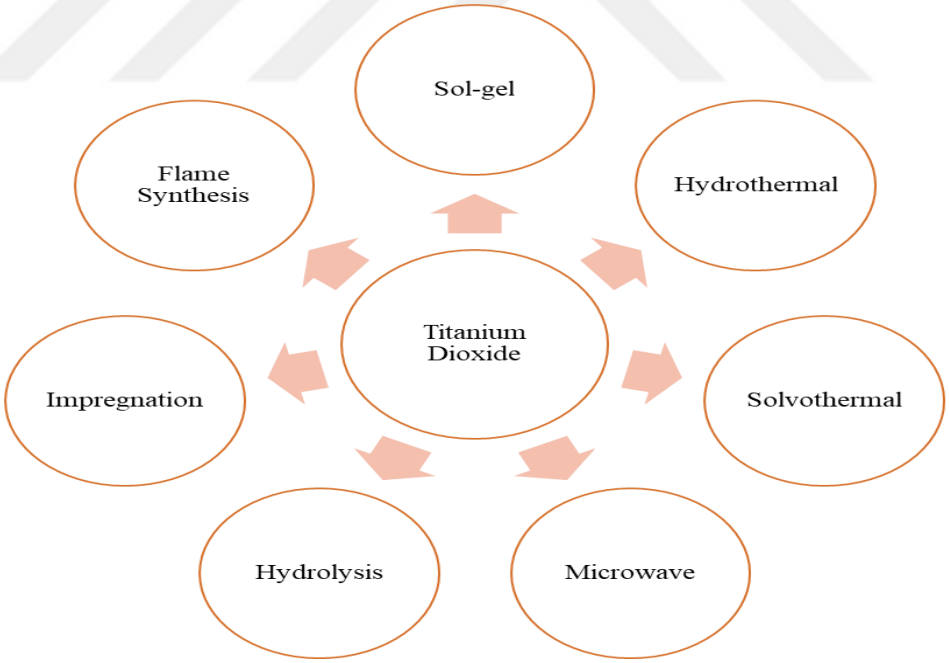

Figure 1.3 Some of the methods used for manufacturing of titania.

All the manufacturing processes mentioned above, except flame synthesis, are wet processes. The disadvantages of wet processes can be summarized as:

1-They need several steps to get the final product such as mixing chemicals, calcination, grinding, washing, filtration and drying.

2-They are time and energy-consuming. For example, calcination takes from 4 to 20 hours, depending on the type of process and the required product. Other steps could take a whole day or night or sometimes a week like drying in some cases.

3-Washing of the final products requires water and some chemicals like ethanol. Washing with chemicals require special remediation processes for washing chemicals or liquids before disposing them into the environment.

Flame vapore synthesis (FVS) process is one of the flame synthesis processes, requires evaporation of the precursor before injecting it into the burner. This evaporation process requires extra equipment and energy for evaporation of precursor consequently, it takes more time and energy for production. Furthermore, it produces undesirable characteristics in morphology and size of the products under low rates of combustion enthalpies [77]. Unlike the other processes, FSP requires less time and energy, fewer chemicals for preparing precursor, no further treatment or post-treatment for the products after manufacturing, and there aren't any disposals left after the end of the process. As it is presented in section 2.1 below.

2.1 Flame Spray Pyrolysis (FSP) Process

The increasing need to produce nanoparticles in a cheap and scalable method and controllable structural properties are the reasons why new researches are focusing on inventing new production methods. Flame spray pyrolysis is a synthesis method which was developed recently to produce nanoparticles in laboratory scale. With its simplicity, scalability, and flexibility in producing a wide range of nanoparticles with different sizes tempted some of the leading catalyst and chemical manufacturer companies like DuPont, Evonik(previously Degussa), Ishihara, Cristal and other companies to rely on it in producing millions of tons of nanoparticles [77]. FSP process has some advantages over the other conventional methods used in nanoparticles production, such as making the product with one step without further processing or post-treatment. It also has flexibility in handling a wide range of precursors, and it is a time-effective method [78]. Liquid metal precursors are made by mixing liquid or solid metal precursors like nitrate, acetate, chlorides, or alkoxides with suitable

solvents like alcoholics, carboxylic acids, and xylenes. The mixed solution must have a high combustion enthalpy with a suitable melting/ decomposition temperature, miscibility, and chemical stability to form particles with the desired structural properties [77]. Figure 1.4, shows the mechanisim of formation of particle from a droplet in FSP process.

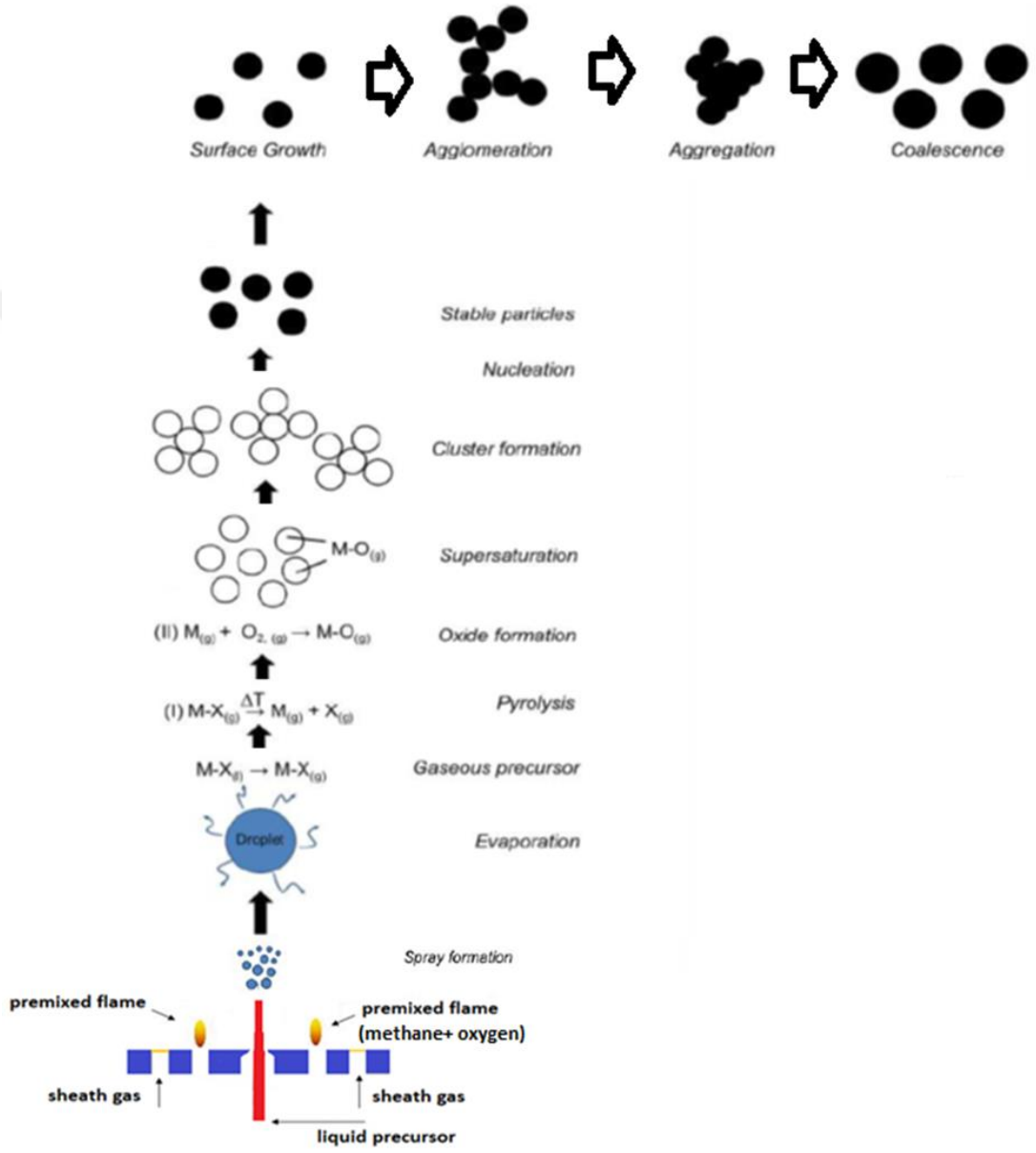

Figure 1.4 Particle formation in FSP process [79].

The production process is initiated when the liquid precursor is injected into a capillary tube inside the nozzle needle, where it will be atomized or dispersed when it is at the other end of the nozzle needle with the support of dispersion oxygen. The

atomized fuel and precursor droplets, with the assist of premixed flame (methane + oxygen) from the flame annulus around it, vaporize/ decompose to form vapors, nucleate, grow by coalescence and sintering. The formed particles are aggregated (chemically bond to create hard agglomerates) and agglomerated (physically bond creating soft agglomerates). With the support of sheath gas and vacuum pump, the formed particles will be pushed and pulled up to the high-temperature resistant aerosol collector where it will be collected [79]. These nanoparticles collectors are made to be highly porous media; they could be glass fiber filters [80], or PTFE- coated fiber bag type filters [81]. The shape and properties of the final products depend on the operating conditions.

3. Modification of Titanium Dioxide with Other Materials

3.1 Coupling

Coupling of semiconductors is another solution to enhance titanium dioxide photoactivity. It is an attachment of two or more semiconductors different in their band gap and electronegativity, but they are not chemically bounded [82]. It can be accomplished by some processes like co-precipitation [83], ball milling [84] and impregnation [85]. The differences in band gap and electronegativity of coupled semiconductors are crucial to induce the transportation of electrons and holes. The heterojunction of semiconductors (coupling) has been reported to be very useful in utilizing visible light and UV and suppresses the electron-hole recombination and increases the charge carriers' lifetime, science the recombination wastes energy. Electron transportation in the coupled nanoparticles is from the lower Fermi level (higher electronegativity and smaller band gap) semiconductor to the higher Fermi level one (lower electronegativity and wide band gap) [86]. Researches proved that the possibility of using coupled photocatalysts in hydrogen production, reduction of carbon dioxide to produce methane and methanol, sensors applications [87] in the degradation of dyes [85] and the reduction of heavy metals [88]. Figure 1.5 depicts a schematic representation of coupling of TiO_2.

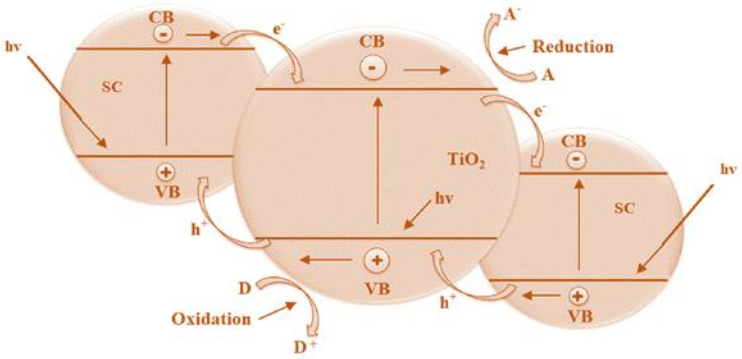

Figure 1.5 Schematic representation of coupling of TiO_2 with semiconductors (SC) [89].

The major disadvantages of coupling are the occurrence of photo-corrosion that make the catalyst less stable and durable and need to add some materials for preventing or delaying it. Moreover, it is not easy to find the suitable semiconductors that give the best results in charge separation and activation under visible light energy [89].

3.1 Dye Sensitization

Dye sensitization means activation of the oxidation-reduction reactions on the surface of titanium dioxide under visible light by using a dye that works as a light harvester and an electron donor. It is a technology that has found its way in developing solar cells to generate electricity [90], water splitting to produce hydrogen [91], and CO_2 photoreduction for methane production [92]. But this technology is not applied widely in the industry due to the low efficiency that is still under research to enhance or develop it [93, 94].

The dye is a component that is responsible for the absorption of the light. The dye should be luminescence, able to cover a light spectrum from UV to visible light, its highest occupied molecular orbital positioned is lower than the conduction band of the TiO_2, and lowest unoccupied molecular orbital should be higher than the conduction band as near as possible to the TiO_2 surface, it must have a hydrophilic periphery, and able to fast electron injection [93]. Organic dyes used in dye sensitization are commonly complexes of metals with low lying excited states. The center of dye involves ruthenium II, zinc II, aluminum III, iron II, and magnesium II,

while the ligands contain heterocyclic nitrogen with a delocalized or aromatic ring system [95]. However, dye sensitization has more disadvantages in addition to its low efficiency, such as instability, dye degradation, and forming undesired products like intermediates [96, 97]. Representation of the possible mechanism for the dye sensitization of TiO_2 is shown in Figure 1.6 below.

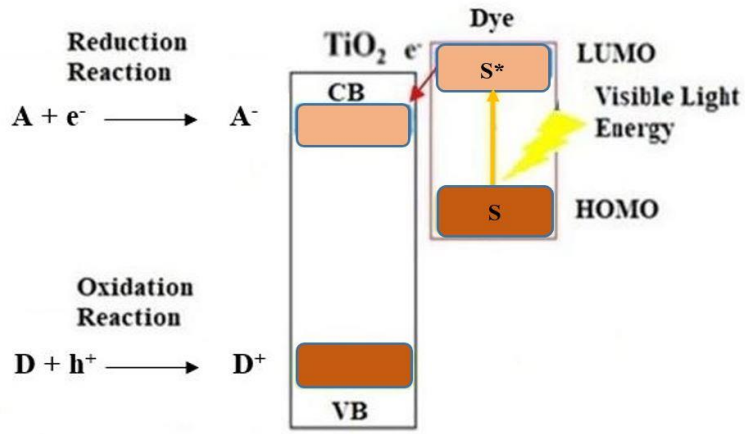

Figure 1.6 Representation of the possible mechanism for the dye sensitization of TiO_2.

3.3 Doping

Doping of titanium dioxide is a process aim (just like the processes mentioned above) to modify titanium dioxide photocatalytic activity and performance, by prolonging the charge separation to avoid or minimize rapid recombination and giving it the advantage of working under visible light [98]. Doping involves the insertion of metals or nonmetals inside the lattice of titanium dioxide. This introduction of dopants can happen in three ways:

- Dry mixing: solid-state reaction method is done by mixing the powder of titanium dioxide with the dopant´s powders [99, 100].
- Wet impregnation: dry titania powders are mixed with a solution involving the dopant materials such as solutions of dissolved salts of acetate or nitrate or metal alkoxides [101].
- Molecular-level mixing is the most common and widely used way. It involves the introduction of dopants and titanium into the reaction in their soluble forms or as

a solution, like titanium IV isopropoxide with the solution of soluble dopants and mixing them before starting the manufacturing process [102].

If the insertion of dopants into the host material´s lattice involves putting the impurity atom in the regular lattice sites, it is called substitutional doping. It happens when the atomic radii difference between the atoms is less than 15 %, the similarity between the dopant and host materials in the crystal structure and electronegativity or comparable valances [103]. In this case, an atom in the lattice is forced out from its site into the voids between atoms. Contrarily, if the dopant atom locates between the normal lattice sites of the host material, it is called interstitial doping. The atomic differences between the dopant and the host play a significant role in this case; the vast difference between them pushes the dopant to put itself in an interstitial position [104].

The change in titanium dioxide properties as a result of doping comprises changes in electrical properties, which are due to the disturbance of the chemical bonding among atoms and distortion of geometric arrangement of them [105]. Moreover, this change in the properties of TiO_2 modifies the degree of crystallinity. It may causes phase transformation from anatase to rutile and growth or reduction of particle size in some cases depending on the type of dopant and preparation process [106].

Titanium dioxide is doped with a wide range of materials such as metals nonmetals and metalloids. Transition metal cations are very popular in doping titanium dioxide, and they are used widely in its applications. They showed good results in suppressing or decreasing the recombination of electron-hole, giving the photocatalyst the ability to work under visible light and increase its photoactivity by enhancing the charge carriers' movement and its surface properties. This enhancement is because the transition metals can form additional energy levels within the band gap of the photocatalyst, which makes the photonic energy needed for the electron transportation from the valance band to the conduction band lower. Sun et al. reported that transition boosts the photocatalytic activity of TiO_2 by a trait of displaying two or more oxidation states differing by one [107]. For example, the recombination of photogenerated electron-hole is inhibited effectively because of the ability of iron to make Fe^{4+}/ Fe^{3+}/ Fe^{+2} ions which work as traps for the photogenerated charge carriers [108]. Zhang et al., in a systematic study, show the importance of similarity in ionic radii between Ti^{4+}

(0.75Å) and Fe^{3+} (0.79Å) for charge carriers trapping [109]. Zafar et al. [110], on their work about manufacturing of Fe/TiO_2 nanotubes and testing their photoactivity under visible light, they used Congo red dye to confirmed the previous results experimentally. In a study on the effect of Ce addition on the characteristics of TiO_2 nanoparticles, Makdee et al. reported the effect of the existence of Ce^{3+} and Ce^{4+} on enhancing the photocatalytic activity by making new energy levels beneath the conduction band of TiO_2 and prevent the electron-hole recombination [111].

Many researchers have reported the effects of cationic dopants on both phase transformation from anatase to rutile and the growth inhibition or promotion in their experiments. Hanaor & Sorrell, categorized in their review the cations into two groups according to their effects on inhibition or formation of rutile phase depending on the experimental data from other studies [112]. They reported that the transformation from anatase to rutile is ascribed to the valance and ionic radius, and their effects on oxygen vacancies. The cationic doping that accompanies with the formation of more oxygen vacancies tends to make phase transformation.

Anions like N, C, S and F [113] are used as dopants for titanium dioxide as well. Mixing of p-state of them with the O 2p of titania make the band gap of titania narrower owing to the shift in the valance band edge upwards minimizing the energy required to activate the electrons to migrate into the conduction band. Creating recombination centres are less than those created by cations. Consequently, they enhance the photocatalytic activity of titania [114]. Neverthless, because the quantum efficiency of anions doped titanium dioxide is still low they are not favoured in photocatalytic applications. The new studies use them with metals to co-dope titanium dioxide [114].

1.2.4 Copper doped Titanium Dioxide

The material used to be as a dopant for titanium dioxide must give it better characteristics as a catalyst. It also must be cheap and available as mentioned above. Regarding the depleting resources and high cost of some metals and the limited resources of the others, developing an efficient catalyst from earth-abundant, with low price, is not optional. Still, it is a necessity for many applications that require the incorporation of a catalyst to avoid high production costs [115]. Copper, one of the

most used metals by humans for centuries, is an outstanding candidate due to its relatively high catalytic performance and low cost. It was found in many studies in the literature that it gives better characteristics when it is doped with other semiconductors. It is doped, co-doped, or coupled with other semiconductors or metals to make better catalysts like doping it with TiO_2, as reported previously, ZnO [116], WO_3 [117] and ZrO_2 [118]. Copper oxide has a narrow bandgap (cupric oxide, 1.4 eV; cuprous oxide, 2.2 eV), which has a high-absorption coefficient, but suffers from UV-induced photo corrosion [119]. However, copper oxide, coupled with TiO_2, has been confirmed as stable, nontoxic, better photocatalytic degradation properties [87]. It was found that it extends its application to the visible region, minimizing the photonic energy needed for electron activation, extending the lifetime of electron-hole separation, and it gives a synergistic effect for the catalyst or photocatalyst by increasing its efficiency, this is because of the similarity in ionic radius between copper and titanium (0.72Å for copper and 0.68Å for titanium) which proposed to make substitutional doping or replacing Ti in the titanium dioxide lattice, and the ability of copper to exhibit more than one ionic state (Cu^{2+} and Cu^{+}) that will help in preventing electron-hole recombination [120]. Tsai et al. prepared Cu/TiO_2 by plasma torch method, and they used the manufactured catalyst for low- concentration mercury removal in the gas phase. They reported the effect of copper through its ability to form Cu^{2+} and Cu^{+} to suppress the electron-hole recombination and provide more holes for Hg reduction/oxidation reaction [121]. Copper is used as a dopant for titanium dioxide in nearly all of the photocatalytic applications like CO_2 photo-reduction, water and air purifications, and solar fuel production. Copper doped titanium dioxide is also used in some applications like batteries, as previously mentioned in the introduction.

CHAPTER 2

2. METHODOLOGY OF SYNTHESIS AND CHARACTERIZATION

2.1 Preparation of Precursors

The materials used in the synthesis of pure and copper doped titanium dioxide are listed in Table 2.1. Titanium (IV) isopropoxide (TTIP) was chosen as a liquid source of titanium. It has a high combustion enthalpy and can be used with a wide range of solvents. Ethanol was used as a cheap solvent that does not lower the enthalpy of combustion for TTIP much, and can mix easily with it making a homogeneous solution. It also improves the breakup of droplets during atomization process. Copper (II) acetate (solid) was used to provide copper for copper doped titanium dioxide products. It was used instead of the widely used copper nitrate as it doesn't make precipitates inside the nozzle. Propionic acid was used in small amounts to dissolve copper (II) acetate.

Table 2.1 Precursor and solvents used in the experiments.

Precursor contents	Brands and Purity
TTIP	TTIP sigma Aldrich, 97 %
Ethanol	isolab, ≥ 99.9 %
Propionic acid	Sigma Aldrich, ≥ 99 %
Copper II acitate	Fisher, 99 %

Pure titanium dioxide was manufactured from a precursor containing only TTIP and ethanol. TTIP was mixed with ethanol to make a 0.5 M solution. The mixture was stirred in a closed beaker to avoid contact with air since TTIP is sensitive to moisture and water as it hydrolyzes. 5 % and 10 % mole copper doped titanium dioxide (Cu/TiO_2) were manufactured using two different amounts of copper (II) acetate (5 and 10 mole %) dissolved in propionic acid. The two mixtures are then mixed with a 0.5 M solution of TTIP and ethanol separately, keeping both of them under stirring until they make a homogeneous solution.

2.2 Production Process

The FSP system shown in Figure 2.1, designed and manufactured as part of a TUBITAK project, was used. FSP process has been chosen for its unique characteristics over the other processes, like wet and FVS processes. Wet processes involve several time consuming steps, and they are not cost-effective. FVS process requires volatile precursors and more energy as previously mentioned in Chapter 1.

Figure 2.1 Flame spray pyrolysis system (FSP) in Dr. Machin's research laboratory.

FSP was performed by using a closed chamber. The working parameters were set to be the same for each batch to produce the nanosized materials under the same conditions. The system was warmed to reach a steady-state by combusting ethanol to heat the chamber. Later the precursor solution was injected into the flame. The exhaust gases were withdrawn via a vacuum pump. The products were filtered out from the combustion gases at the top of the chamber by a glass fiber filter (Whatman GF/D, 257 mm diameter), which was then removed from the system at the end of the production batch to collect the formed nanopowder. The operating parameters are listed in Table 2.2. The resultant pressure drop from the used GLFR and the used distance ring (3.01 mm) in the nozzle is 0.3 bar. Nanoparticles collected from the filter were sent to the several central laboratories for the previously mentioned analysis for characterizations.

Figure 2.2 represents the schematic representation of FSP process used in the production of nanoparticles for this thesis.

Table 2.2 Operating parameters used in the production of pure and copper doped titanium dioxide in this work.

Type of material	Flowrate
Precursor liquid flow rate (ml/min)	3
Oxygen dispersion gas (L/min)	15
Shield gas (air) (L/min)	10
Methane to burner (L/min)	1
Oxygen to burner (L/min)	1

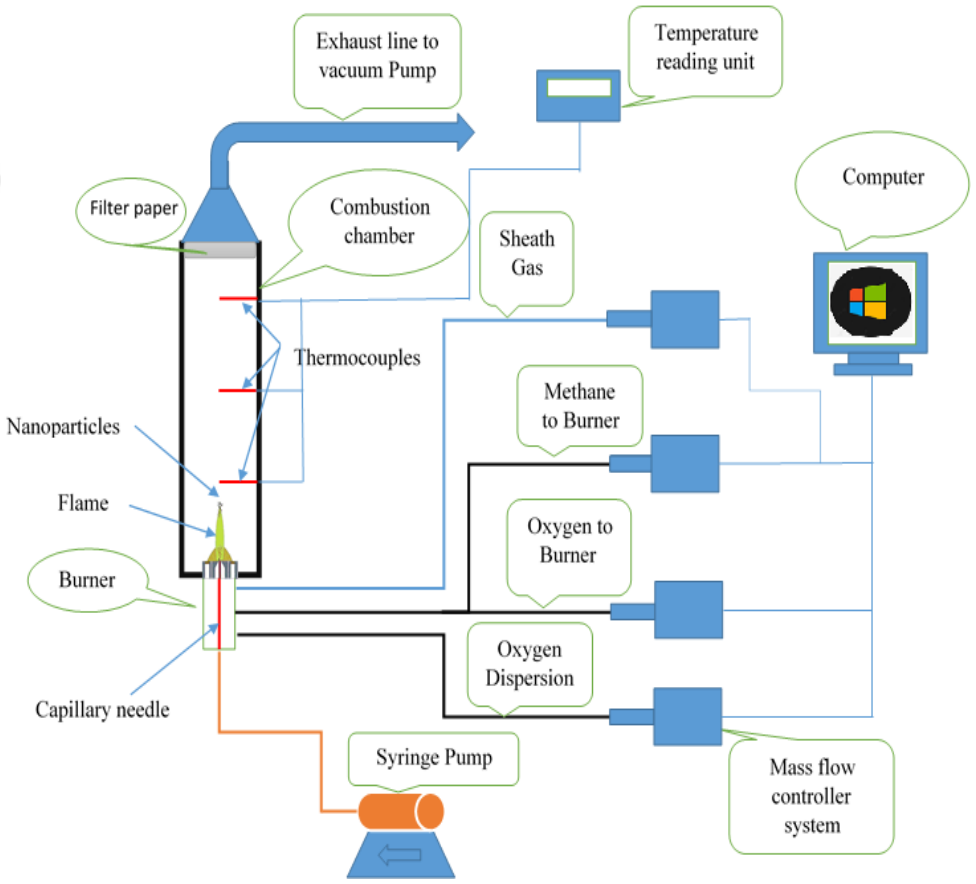

Figure 2.2 Schematic representation of FSP.

Figure 2.3 below shows the produced nanoparticle before collecting them from the surface of the GF/D filter papers, and in the sample tubes. The change in the color of the products with the addition of copper can be observed in b and c.

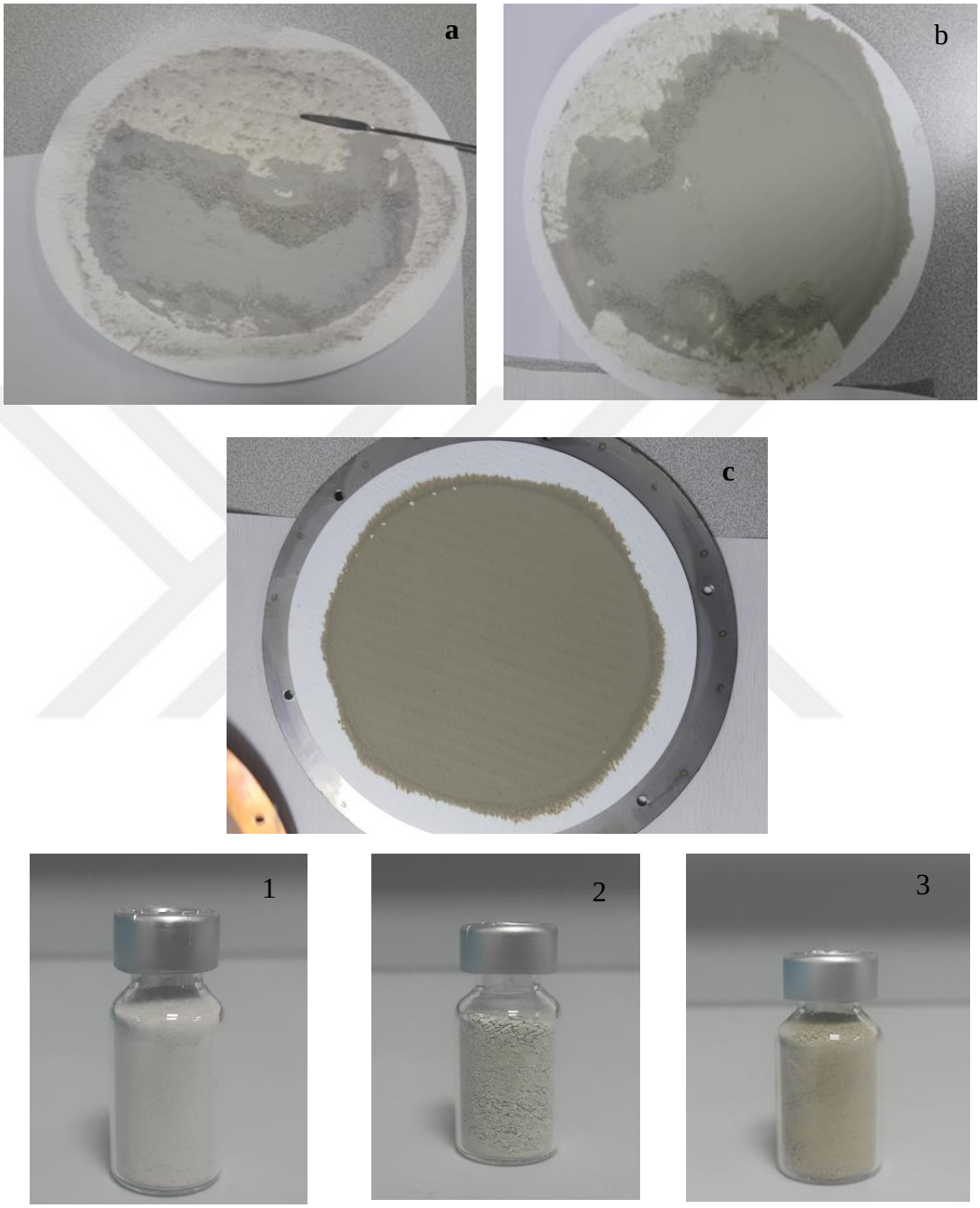

Figure 2.3 Appearance of the final product powders on the Glass fiber filter (GF/D) and after collecting them into tubes, the pictures: a and 1) for pure TiO_2, b and 2) for 5 mole % copper doped titanium dioxide (5 mole % Cu/TiO_2), c and 3) for 10 mole % copper doped titanium dioxide (10 mole % Cu/TiO_2).

2.2 Characterization of the Products

2.3.1 X-ray Diffraction (XRD)

X-ray diffraction is a powerful method for figuring out the atomic arrangements in the matter. It has many applications, including differentiation between crystalline and amorphous phases, determination of the structure of crystalline materials, and determination of single crystals' orientation [122]. Single-crystal XRD method can be used to quickly determine the crystal structure of a material of interest. The sample preparation requirement is a major limitation to this technique since many crystalline materials cannot be prepared for a single crystal XRD analysis as a crystal of appropriate size and quality [122].

The polycrystalline powder sample means it consists of a vast number of randomly oriented single crystals [123]. Throughout the performing the XRD analysis, the applied X-rays on the targeted sample scatter in different trajectories depending on the orientation of the atoms in the crystal. The emitted radiation scatters with a significant intensity only in certain specific directions; the intensity is zero in all other directions. Because the wavelength of X-rays and the spacing among layers of atoms (d) are similar (0.5 to 2.5 angstroms), the intensity peaks can be measured [124]. Using the position and the size of the peaks, the crystal structure and chemical composition for a mineral can be characterized since every sort of mineral shows a unique set of peaks. The collective X-ray scattering from a powder sample gives rise to a set of coaxial cones of scattered radiation. The XRD pattern for a specific powder consists of the measured diffracted intensity as a function of each cone's semi-angle, called the diffraction angle, 2θ. Because of this, the 3D information in the diffraction data is "compressed" into one dimension. The peaks in the pattern arise at specific values of 2θ that satisfy Bragg's law below [124]:

$$2\theta_{hkl} = 2\ sin^{-1}\left[\frac{\lambda}{2d_{hkl}}\right] \quad (1)$$

where λ is the wavelength of the X-rays, d is the interplanar spacing in between the planes of atoms, and the indices h,k, and l are called the Miller indices, which uniquely label each peak (intensity maximum) in the diffraction pattern.

The sample needed to be examined by the XRD is prepared by pressing it into a holder, so it has a smooth surface and placed in the sample chamber. X-ray is created from the bombardment of a metal (e.g., copper or cobalt) with high-energy photons. By using a goniometer, the instrument scans the sample between the desired starting and ending angle. A simple illustration of the inside design can be seen in Figure 2.4. The device directs the X-ray beam, sample, and detector in such a way that suitable conditions to meet the Bragg's equation are maintained.

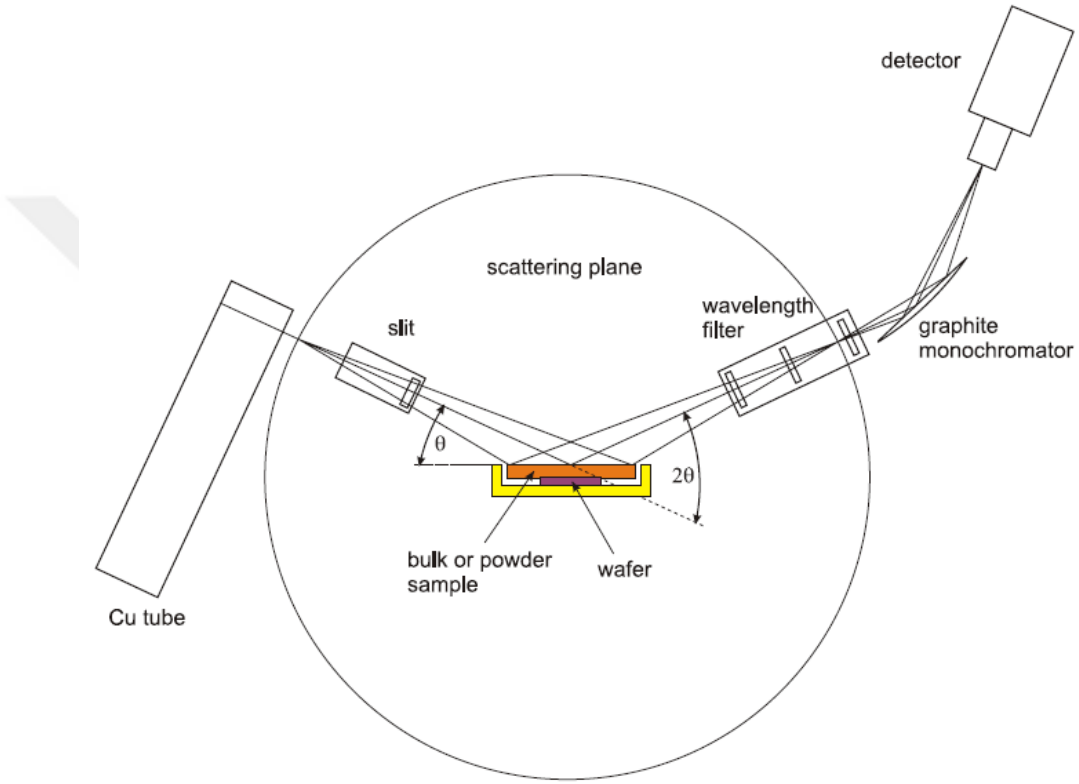

Figure 2.4 A simple schematic illustration of the internal design of X-ray diffractometer [125].

To characterize the three manufactured powders of this work by XRD, analysis was done by using Rigaku Ultima IV X-ray diffraction, Cu/40kv/30 mA radiation,0.5 degrees/min scan speed, and 10° to 90° scan range, in the central laboratory of Middle East Technical University/Ankara. For identification of crystal structure, the joint committee on powder diffraction standard- international center for diffraction data (JCPD-ICDD) system has been applied. The percentage of rutile will be calculated by using Spurr and Myer equation [126] below.

$$X_r = \left[1 + 0.8\frac{I_a}{I_r}\right]^{-1} \quad (2)$$

where X_r is the volume fraction of rutile phase, I_a and I_r are the highest intensities of anatase and rutile phase respectively. Debye-Scherer equation is used to estimate the average crystal size.

$$d = \frac{0.9\lambda}{\beta cos\theta} \quad (3)$$

In equation 3, 0.9 is Scherrer constant, d is the particle diameter, λ is the wave length of X-Ray (0.15406 Å), β is the FWHM (full width at half maximum), θ is the Bragg angle.

2.3.2 N_2 Adsorption-Desorption Analysis

It is one of the commonly used analyses for the characterization of nanoscale particles. It provides the necessary data to estimate the surface area and the porosity of nanomaterials, which are considered unique properties compared to their bulk counterparts [127]. N_2 adsorption-desorption analysis is commenced by exposing the solid sample to a combination of heat, vacuum, and flowing gas to remove the undesired adsorbed contaminants acquired from atmospheric exposure. The sample is then cooled under vacuum, usually to cryogenic temperature (77 K). An adsorptive gas, usually nitrogen, is presented to the pretreated sample is controlled, steadily increasing doses. The pressure is allowed to equilibrate after each dose, and the amount of gas adsorbed is calculated. The volume of the adsorbed gas at each dose and one constant temperature expresses an adsorption isotherm, which allows determination of the quantity of gas required to form a monolayer over the solid and its pores' external surface. Covering the sample surface by a known amount of adsorbed gas molecules makes it possible to calculate the surface area of the solid sample [128]. There are different data reduction methods; one of them is the Brunauer, Emmet, and Teller (BET) method, which determines specific surface area (SSA) on a model of adsorption which incorporates multilayer coverage of the solid surface by the adsorptive. When the area of the interface between two phases is proportional to the mass of one of the phases (e.g., for a solid adsorbent), dividing the surface area by the mass of the relevant

phase gives the SSA area (Equation 4) [127]. The porosity of the sample can also be known from the shape of the formed hysteresis isotherms and the size of the pores.

The samples from the manufactured powders of this work were outgassed at 250℃ for 2 hours before starting tests Nitrogen at 77.4 K was used. The analysis time was 406.9 minutes for pure TiO_2, 579 minutes for 5 % Cu/TiO_2, and 627 minutes for 10 % Cu/TiO_2. The device used for this analysis is the AUTOSORB-1C/MS, in the central laboratory of Middle East Technical University/Ankara. Particles sizes were calculated according to the equation:

$$d_{BET} = \frac{6000}{[X_r * \rho_r + X_a * \rho_a] * SSA} \quad (4)$$

where X_r is the rutile phase percentage in the sample, ρ_r is the density of the rutile phase, X_a is the anatase phase percentage, ρ_a is the density of the anatase phase, SSA is the specific surface area.

2.3.4 Scanning Electron Microscopy (SEM) Analysis

It is a magnification tool that uses the electron beam to provide visual images about materials. Unlike the TEM the electron scattering captured by a detector is used to make these images, not the transmitting electrons. These images give information about the shape and the surface of the material. It consists as in Figure 2.5 of the same parts that the TEM has, except that it doesn't have an objective, aperture, and projection lenses. Moreover, it doesn't have the Fluorescent screen that TEM has. SEM can provide images with lower magnification than TEM can provide [129]. The reason the resolution of the SEM is lower than that of the TEM is that the electrons' wavelength is longer because the accelerating voltage of the electrons used in the SEM is as low as several kV to several tens kV. Besides, the characteristic difference of the electromagnetic lenses used to converge the electron beams [130].

SEM instrument used to get the SEM images for the three produced samples of this study is Quanta 400F field emission SEM is the device used to analyze the samples produced, in the central laboratory of Middle east Technical university.

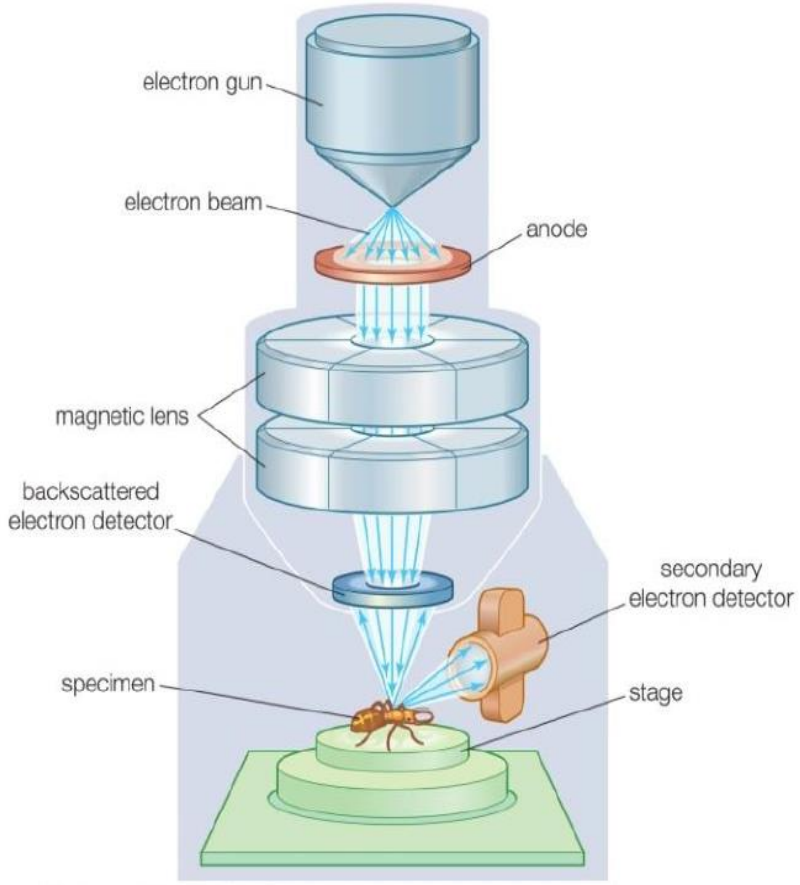

Figure 2.5 Scanning electron microscope system illustration [129].

2.3.3 Transmission Electron Microscopy (TEM) Analysis

It is a powerful and important instrument engineered tool (Figure 2.6). As its name suggested, TEM, it uses the transmitted electrons that passing through the material and then collected. It provides information about different materials at a very high spatial resolution, including particle size, crystallinity, morphology, chemical constituents, and phases. It consists of the following basic systems [131] :

(1) Emitting and the condensing system is responsible for producing a beam of electrons and focusing it onto the sample to be examined. An electron gun is responsible for emitting electrons. It includes two parts; a filament that is a thin wire mostly made of tungsten and an anode that is a plate of metal placed some centimeters underneath the filament. The condensing system is used to focusing or centering the emitted beam of electrons from the electron source with the aid of its magnetic lenses.

(2) The image- formation system, to form or produce images, involves the objective lens, a mobile stage where the samples are put, and an intermediate and projector lens that focuses the electrons that pass through the specimen or sample to form a real, highly magnified image.

(3) The image recording system, to transform the image of an electron into some form that is perceptible to the human eye. It usually consists of a fluorescent screen to display and focus the image, and a permanent recording digital camera. Additionally, it requires a vacuum system consisting of pumps and their associated gauges, valves, and power supplies.

The machine used for TEM and HRTEM analysis of the samples produced for this study is JEOL 2100F HRTEM 200KV, in the central laboratory of Middle East Technical University/Ankara. Image J software was used to estimate the particle sizes, average particle size distribution, and d-spacing from TEM pictures.

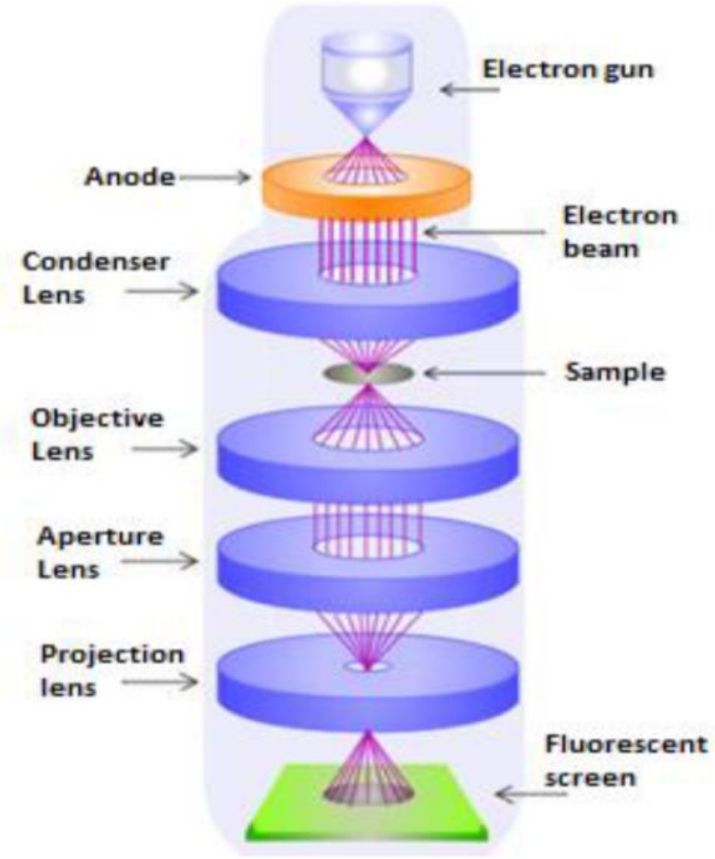

Figure 2.6 Transmission electron microscope system illustration [131].

2.3.5 UV-vis Diffuse Reflectance Analysis

It is well-known that light cannot penetrate solid materials; it reflects on their surfaces. Accordingly, the light reflection on the solid surfaces can be categorized as specular and diffuse reflection. Specular reflection is an asymmetrical reflection with respect to the regular line, while, diffuse reflection happens as a result of light scattering in different directions [132], as shown in Figure 2.7.

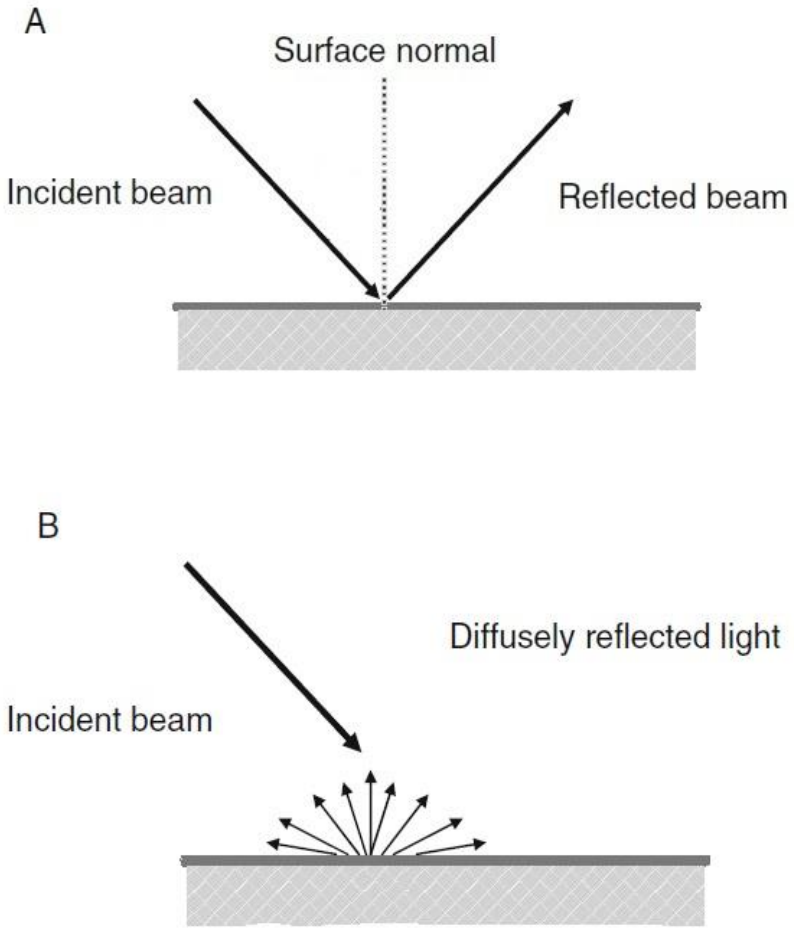

Figure 2.7 (A) Specular reflection, (B) Diffuse reflection [133].

In the UV-vis Diffuse Reflectance spectrophotometer, the sample is put in front of an incident light window to accomplish the measurement. The reflected light from the sample is then concentrated on a detector by a sphere called the integrating sphere,

which is coated with barium sulfate from inside. The percentage of incident light beam absorbed by the testing sample can be calculated from the relation [133] :

$$\% \text{ Absorbance} = 100\% - \%R - \%T \quad (5)$$

where %R : is the percentage of the diffused reflectance of the beam of light.

%T : is the percentage ofthe diffused transmittance of the beam of light.

The bandgap of a semiconductor can be estimated from the absorbance data provided by the UV-vis Diffuse Reflectance analysis. The bandgap energy is the energy required to make the electron jump from the valance band which is filled with valance electrons to the conduction band that is completely empty.

Tauc plot is the widely used method to calculate the band gap. The process of measuring can be done using the following [134, 135]:

1- Tauc, Davis and Mott relation

$$(h\nu\alpha)^{1/n} = A(h\nu - E_g) \quad (6)$$

here:

h: Planck's constant, ν: frequency of vibration, α: absorption coefficient, Eg: band gap, A: proportional constant

The exponent n denotes the nature of the sample transition; its value is considered as follow:

For direct allowed transition····· n = 1/2

For direct forbidden transition····· n = 3/2

For indirect allowed transition····· n = 2

For indirect forbidden transition····· n = 3

Because the direct allowed sample transition is the most used to express the TiO_2 band gap, n = 1/2 is used to calculate the band gap for the samples in this work.

2- The acquired diffuse reflectance spectrum is converted to the Kubelka-Munk function. Thus, the vertical axis is converted to quantity F(R∞), which is proportional to the absorption coefficient. The α in the Tauc equation is substituted with F(R∞). Thus, in the actual experiment, the relational expression becomes:

$$(h\nu F(R\infty))^2 = A(h\nu - Eg) \quad (7)$$

3- Using the Kubelka-Munk function, the $(h\nu F(R\infty))^2$ is plotted against the hν. The curve that plots the value of $(h\nu - (h\nu F(R\infty))^2)$ on the horizontal axis hν and the vertical axis $(h\nu F(R\infty))^2$ is drawn. Here, the unit for hν is eV (electron volts), and its relationship to the wavelength λ (nm) becomes $h\nu = 1239.7/\lambda$.

4- A line is drawn tangent to the point of inflection on the curve of step (3), and the hν value at the point of intersection of the tangent line and the horizontal axis is the bandgap Eg value.

The device used to get the absorbance and reflectance data for the produced samples of this work is Schimadzu/3600 Plus, under normal laboratory conditions, for a wavelength range from 200-900 nm. The analysis was done in the Uluğ Bey Yüksek Teknoloji Uygulama ve Araştırma Merkezi at Gaziantep University/ Gaziantep.

CHAPTER 3

3. RESULTS AND DISCUSSION

3.1. XRD Analysis

XRD analysis of the products was done in a range from 10° to 90° as previuosly mentioned. Figure 3.1 shows three patterns belonging to three manufactured samples with recognized peaks.

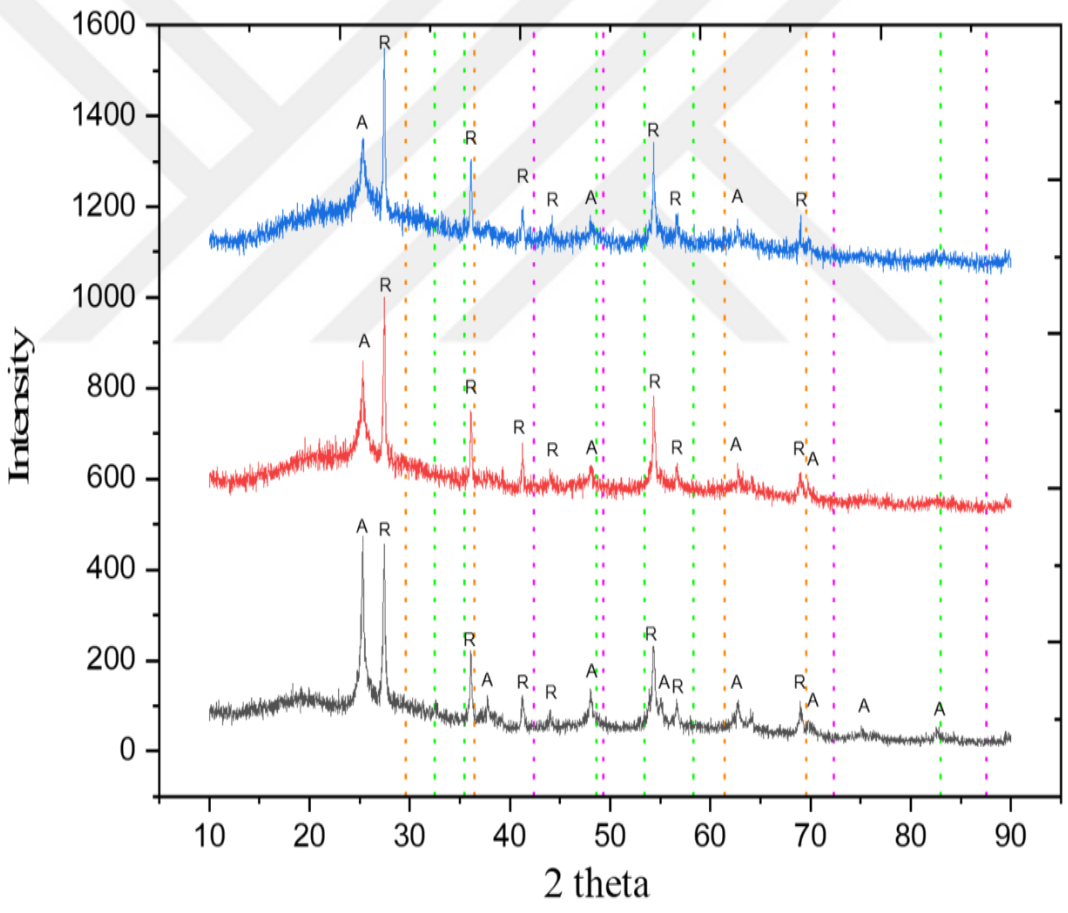

Figure 3.1 X-ray Diffraction patterns of pure titanium dioxide (the black one), 5 mole % copper doped titanium dioxide (the red one) and 10 mole % copper doped titanium dioxide (the blue one). Dotted vertical lines (purple Cu, Green CuO, and Orange Cu_2O). A (anatase), R (Rutile).

From Figure 3.1 above, the black pattern is for pure titanium dioxide, its 2θ values are anatase and rutile phases according to the ICDD card number 021-1272 and ICDD card number 021-1276, respectively. The red pattern is for the 5 % copper doped titanium dioxide, its 2θ values are anatase and rutile according to the ICDD card number 01-075-1537 and ICDD card number 021-1276 respectively. The pattern for 5 % Cu/TiO_2 doesn´t show any peaks for Cu metal or Cu oxides (CuO and Cu_2O). The blue pattern represents the 10 % mole Cu/TiO_2 sample; this pattern reveals 2θ values for anatase and rutile according to ICDD card number 01-086-1157 and ICDD card number 021-1276 respectively. This pattern doesn´t show any peaks for copper metal or copper oxides, just like the red pattern. The dotted vertical lines refer to the positions of the most intense peaks of metal copper, CuO and Cu_2O peaks; they were set according to the Crystallographic Open Database (COD) 9016326 for CuO, COD 9013023 for Cu and COD 9007497 for Cu_2O. The dotted vertical lines for Cu and Cu_2O have no corresponding peaks, proving the absence of these crystals phases in the structures.

Table 3.1 Crystallinity percentages for the manufactured samples.

Sample Type	% Crystallinity
Pure TiO_2	67.5
5 mole % Cu/TiO_2	32.2
10 mole % Cu/TiO_2	24.0

Table 3.1 above, lists the crystallinity percentages for the three samples, and it shows that the crystallinity percentage decreases with the addition of copper and with increasing this addition from 5 % to 10 % (mole) it decreases more. Table 3.2 below shows the 2θ values for the peaks in Figure 3.1 and their corresponding crystal planes for pure and copper doped TiO_2 from the XRD analysis results.

Table 3.2 2θ and Crystal planes for pure and copper doped TiO_2, (A: anatase, R: rutile).

10 mole % Cu/TiO_2				5 mole % Cu/TiO_2				Pure TiO_2			
R		A		R		A		R		A	
Crystal planes	2θ	Crystal planes	2θ	Crystal planes	2θ	Crystal planes	2θ	Crystal planes	2θ	Crystal planes	2θ
110	27.448	101	25.289	110	27.453	101	25.289	110	27.398	101	25.777
101	36.099	004	37.785	101	36.079	103	37.834	101	36.079	103	37.751
111	41.282	200	48.107	111	41.235	200	48.073	111	41.203	200	48.010
210	44.124	213	62.622	210	44.152	211	54.934	210	43.980	211	54.970
211	54.320			211	54.347	204	62.788	211	54.317	204	62.703
220	56.633			220	56.576	116	68.991	220	56.636	220	69.749
301	68.898			310	64.208	220	69.697	310	64.036	107	74.834
								116	68.998	303	82.324

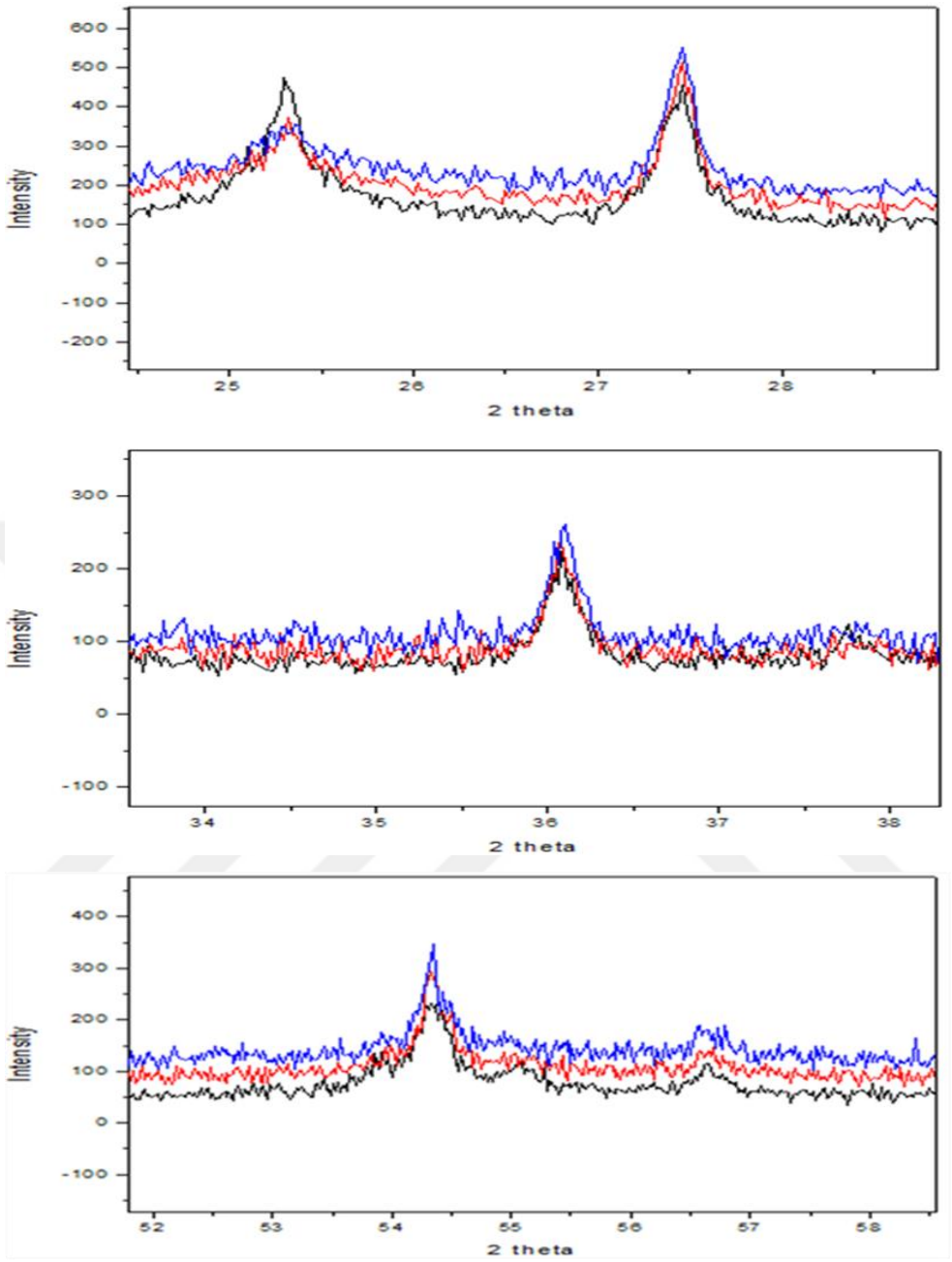

Figure 3.2 The effect of adding copper on diffraction patterns for the most intense peaks. Anatase peaks 25.777, 37.7513, 54.97, Rutile peaks 27.4529, 36.079, 54.31. The black pattern for pure TiO_2, the red pattern for 5 mole % Cu/TiO_2, and the blue one for 10 mole % Cu/TiO_2.

Three things can be noticed in the three patterns shown in Figure 3.1. First, the number of peaks decrease with increasing the dopant content as discussed above. The

black pattern has a higher number of peaks than the red one, and the latter has a higher number of peaks compared to the red pattern, which has the lowest number of peaks. The second, as depicted in Figure 3.2 above, is broadening and shifting of anatase peaks while the rutile peaks are becoming more intense when copper is added, and increased from 5 % to 10 % (mole). The third is the absence of Cu metal and Cu oxides peaks in patterns 2 and 3, where the samples are doped with copper.

The absence of copper metal and copper oxides peaks can be ascribed to the high dispersion of Cu in TiO_2 and the low concentration of copper in the precursor [136]. But, the existence of the large amount of amorphous phase in the samples also indicates that maybe Cu did not crystallize completely [137]. Table 3.3 shows the percentages of rutile in each sample; they were calculated using Spurr and Myer equation. They reveal that the percentage of rutile increases from 55 % for the pure TiO_2 to 63.2 % for the 5 mole % Cu/TiO_2 to 66.07 % for the 10 mole % Cu/TiO_2. The doping effects of copper into TiO_2 was discovered to cause anatase phase transformation into the rutile phase [138], because of substitutional entering of copper atoms into the TiO_2 lattice makes more defects, most likely oxygen vacancies inside the crystal of titanium dioxide [139]. This phase transformation was noticed by researches that investigated the doping of copper [140] and other transition metals like Ce [19] and Fe [18].

Table 3.3 Percentages of anatase and rutile in pure and copper doped titanium dioxide samples and average particle diameter.

Sample	Anatase wt %[a]	Rutile wt %	d_{XRD},average (nm)
Pure TiO_2	45	55	23.68
5 mole % Cu/TiO_2	36.8	63.2	31.87
10 mole % Cu/TiO_2	33.93	66.07	33.3

[a]The anatase percentage were calculated according to 100- rutile % = anatase %

It is worthy to mention here that the high percentage of rutile in the pure titanium dioxide can be ascribed to the high oxygen amount used in the manufacturing processes, this is in a good agreement with the few literature that ascribed the high rutile content in the products to the process parameters not to the doping process only in flame synthsis processes. Ahmad et al. [141] synthesized TiO_2 using chemical vapor synthesis process or FVS process and found the effect of gas flow rate on increasing the amount of rutile with increasing the O_2/He flow rate ratio.

The anatase and rutile phases of the manufactured samples have tetragonal structures. Their lattice and d-spacing parameters, listed in Table 3.4, are in a good agreement with ICDD cards for anatase 021-1272, 01-086-1157, 01-075-1537 space group 141: 41|/amd and ICDD card 021-1276 for rutile space group 136: P42/mnm.

Table 3.4 Lattice parameters and d-spacing of TiO_2, 5 % and 10 % (mole) Cu/TiO_2.

Sample	Lattice parameters, anatase phase	Lattice parameters, rutile phase	d-spacing anatse phase Å	d-spacing, rutile phase Å
Pure TiO_2	$a = 3.7861$ $c = 9.5128$	$a = 4.5947$ $c = 2.9593$	$d(101) = 3.5205$	$d(110) = 3.2525$
5 mole % Cu/TiO_2	$a = 3.8008$ $c = 9.4506$	$a = 4.5958$ $c = 2.9609$	$d(101) = 3.5188$	$d(110) = 3.2462$
10 mole % Cu/TiO_2	$a = 3.7961$ $c = 9.4331$	$a = 4.603$ $c = 2.96$	$d(101) = 3.519$	$d(110) = 3.2467$

3.2. N_2 Adsorption- Desorption Analysis.

Figure 3.3 below illustrates the N_2 adsorption-desorption isotherms for pure and 5 % and 10 % (mole) Cu/TiO_2.

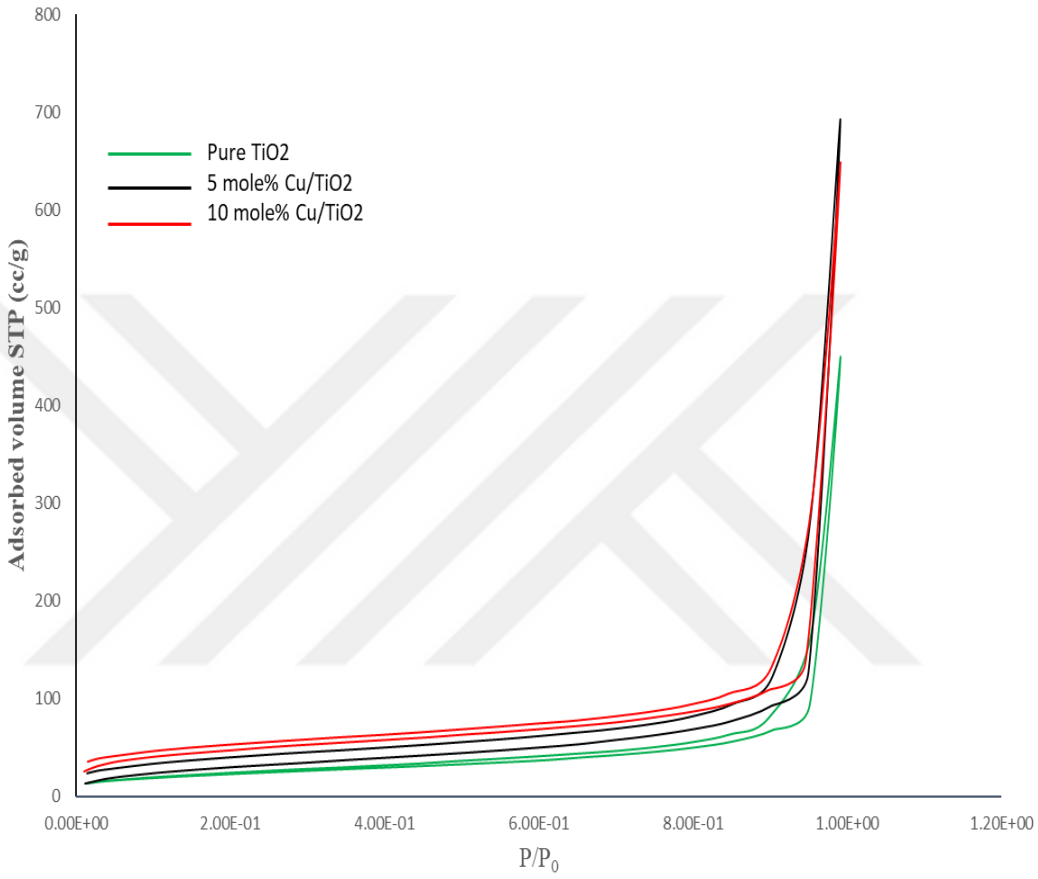

Figure 3.3 N_2 adsorption-desorption isotherms of Pure and Cu doped TiO_2 nanoparticles.

All curves for the previously manufactured samples show type IV isotherm conferring to the IUPAC classification, which indicates mesoporous material, and they show hysteresis loops of H3 type [128]. The occurrence of H3 hysteresis at high relative pressure is due to the capillary condensation of adsorbent (Nitrogen) within the mesopores, usually accompanied by solid materials that constitute aggregates or agglomerates of particles of the slit-shaped pore with nonuniform size or shape [142]. The existence of type IV isotherm and H3 hysteresis are in good agreement with the previous studies that manufactured TiO_2 in a pure or doped forms [143, 144].

Interestingly, the three samples have low-pressure hysteresis (LPH) loops below the anticipated closure value which is 0.42 for nitrogen [145] as follow: the adsorption isotherms for the pure titanium dioxide exhibit a closure point for P/P_o at roughly 0.3, for 5 % and 10 % copper doped titanium dioxide, there are no closure points. The LPH phenomenon has been observed in some literature about manufacturing pure or modified TiO_2 prepared at different manufacturing methods like hydrothermal method [143], FSP process [144], mechanical ball-milling [146] and sol-gel [147]. It is also found in other literatures about nanoparticles and/or porous solids [148, 149, 150]. Despite the observations of the LPH phenomenon in many porous solids, it was rarely discussed. However, the studies that discussed and examined this real physical phenomenon have attributed it to two reasons: equilibration time and outgassing conditions [151, 152]. The desorption branch of isotherm extends to the lowest point of P/P_o for doped samples. Silvestre-Albero et al. [151] have investigated LPH in adsorption by examining the effect of equilibration time and the outgassing conditions on some porous solids. Firstly they investigated the long equilibration time, some materials reached a closure point at values higher than the minimum for nitrogen adsorption ($P/P_o = 0.42$), other materials recorded a lower closure point lower than 0.42, they attributed this difference in closure point values to the irreversible uptake, because some pores have the same width of nitrogen molecules. They also concluded other reason, lack of equilibrium in the adsorption branch, i.e., the occurrence of adsorption of N_2 in narrow micropores at a lower temperature of adsorption measurements limits the accessibility of the adsorbent gas, under these conditions, at 77 K the adsorption branch is under the lack of equilibrium, on the other hand, the desorption branch will be in a good equilibrium circumstance. Secondly, the temperature degree of the thermal treatment used during the outgassing process. They found that all the samples have gotten higher closure points at higher values of P/P_o (over 0.42), and the amount of nitrogen adsorbed was increased as well when they exposed to higher outgassing conditions (higher temperature and longer time). Moisture, volatile species and tar are examples of the materials that block the pores and cause LPH loops.

In any case, the type of isotherm and the hysteresis loop is not changing, neither with long equilibration time nor higher outgassing temperature [151]. The effect of low temperature in the outgassing process was mentioned as a reason for LPH according to the IUPAC report [152].

Table 3.5 shows the effect of loading copper as a dopant into TiO_2. Cu doping increases the specific surface area. It can be concluded that adding copper into the titanium dioxide´s lattice has an effect on increasing the surface area. The particles´ sizes were calculated using equation (4), which assumes all the particles in the sample have spherical shapes and they are homogenous.

Table 3.5 N_2 adsorption-desorption results.

Sample	S_{BET} (m^2/g)	d_{BET} (nm)	Pore volume (cm^3/g)	Pore size (nm)
Pure TiO_2	83.2	17.89	0.7043	1.65
5 mole % Cu/TiO_2	111.2	13.05	1.08	1.35
10 mole % Cu/TiO_2	162.9	9.25	1.001	0.99

BJH analysis has been done to calculate the pore sizes and pore volumes. Table 3.5 above shows the average pore sizes from BJH analysis, and they prove the presence of micropores in the three samples (pore size < 2 nm). BJH pore size distributions are depicted in Figure 3.4 below; from these figures it can be seen that there are peaks at mesoporosity region (2-50 nm) proving the mesoporosity characteristics for the produced samples.

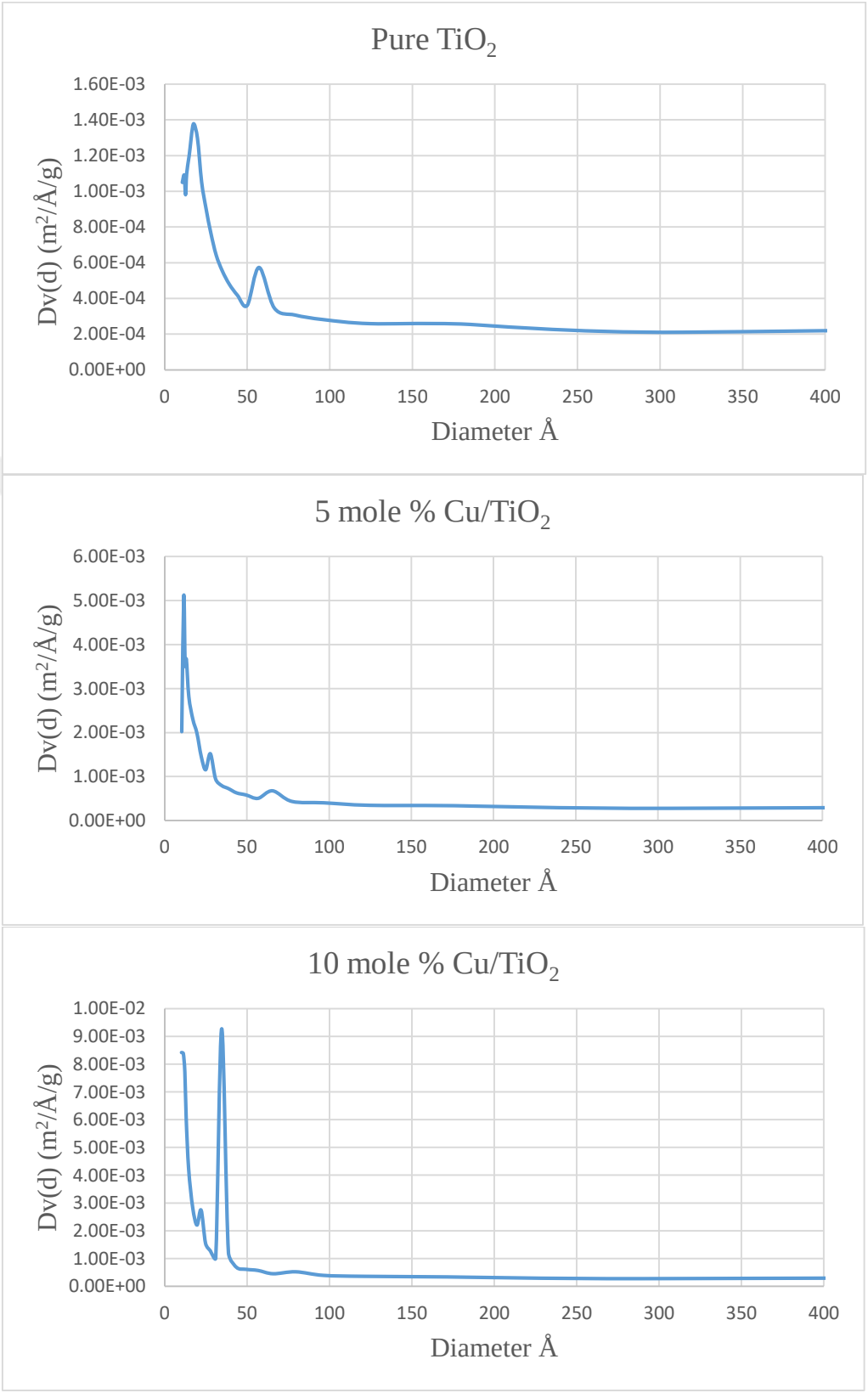

Figure 3.4 Differential distribution of pore size for the manufactured samples.

4.4 SEM Analysis

Figure 3.5 below depicts the SEM images of pure TiO_2, 5 mole % Cu/TiO_2 and 10 mole % Cu/TiO_2, respectively.

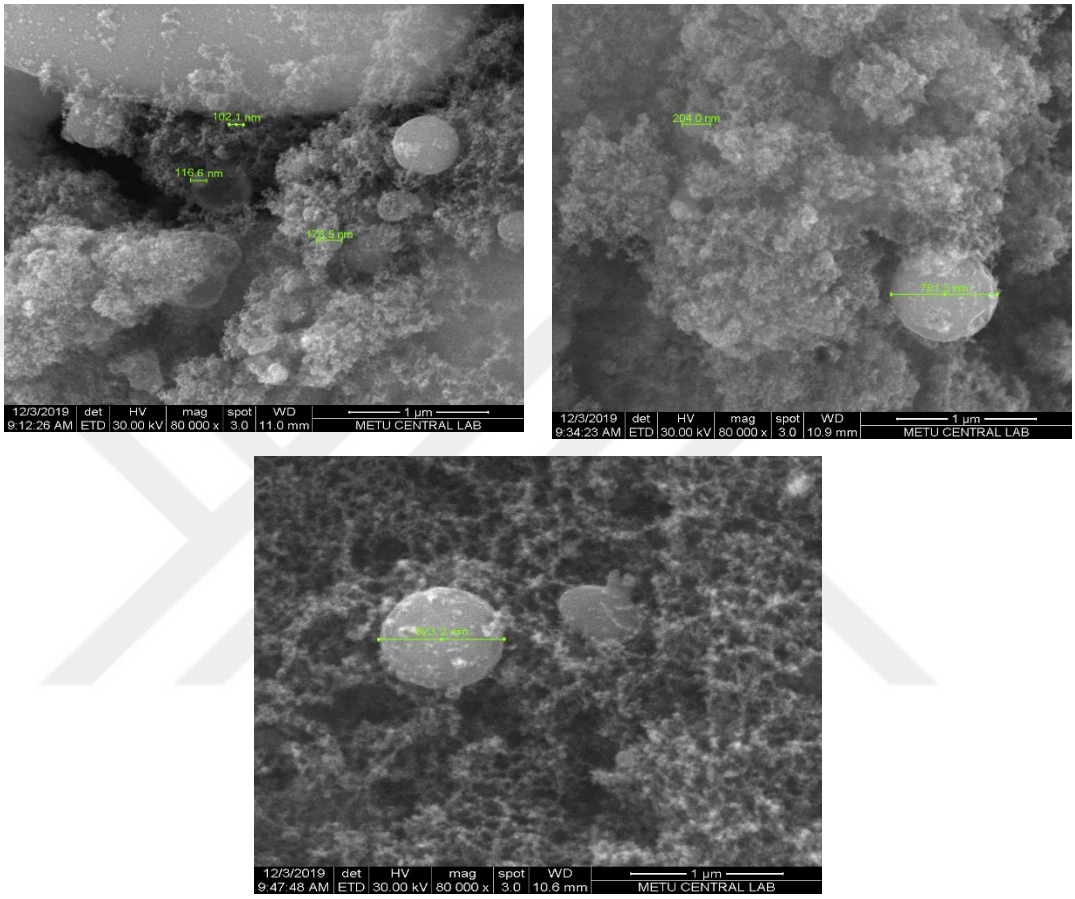

Figure 3.5 SEM images for a) pure TiO_2 b) 5 mole % Cu/TiO_2 and c) 10 mole % Cu/TiO_2.

The above pictures are showing the presence of eggshell structures in addition to the nanoparticles. The existence of these structures normally happens in the FSP process when some droplets do not completely evaporate in the flame and escape from it. This is due to the high GLFR, lower pressure drop (0.3 bar), which results in a short residence time making some of the droplets escape from the flame without being completely evaporated. Moreover, the addition of the copper acetate to the precursor solution lowers the enthalpy of combustion, as in Table 3.6, exposing the droplets to lower heat, which makes the rate of droplets evaporation lower than the case of pure

TiO_2. The enthalpy of combustion becomes less with addition more copper acetate. Consequently, residence time and the low enthalpy precursor (for doped precursors) increase the direct conversion path of droplets into particles. Moreover, it stimulates the formation of more eggshell structures. The formed eggshell structures and solid particles show that under the used production conditions in this work, the system depicts two paths of droplet conversion: droplet to solid and vapor to solid.

Table 3.6 Combustion enthalpies of the components and the precursors of the manufactured materials in this work.

Component	Enthalpy of combustion kJ/ml	Precursors enthalpy of Combustion kJ/ml		
		Pure TiO_2	5 mole % Cu/TiO_2	10 mole % Cu/TiO_2
Propionic acid	20.473			
Ethanol	23.451	23.858	23.526	22.079
Titanium IV propoxide	26.193			

To make a comparison between the size of droplets and the size of the eggshell particles, the droplet size where calculated using Ansys Fluent 19.2 software under the same working conditions (liquid and gas flowrate) but for 0.48 bar pressure drop. The simulation shows that the maximum droplet size is 17 µm. From Figure 3.5 above the maximum eggshell sizes were 175 nm for pure TiO_2, 731.3 nm for 5 mole % Cu/TiO_2, and 823.2 nm for 10 mole % Cu/TiO_2. This comparison shows that the droplets need more time to evaporate which means more residence time is required, or smaller droplets should have been formed by applying a higher pressure drop.

3.3 TEM/ HRTEM Analysis

The pictures in Figure 3.6 show the TEM images of pure TiO_2, 5 mole % Cu/TiO_2, and 10 mole % Cu/TiO_2. The particles in picture (a) are highly agglomerated than the particles in the (b) and (c) pictures. In pictures (b) and (c) some of non-agglomerated particles can be seen but this is not the case in picture (a). The pictures show that the primary particles mostly spherical but they are polymorphous (have different sizes) and also some particles have non-spherical shapes.

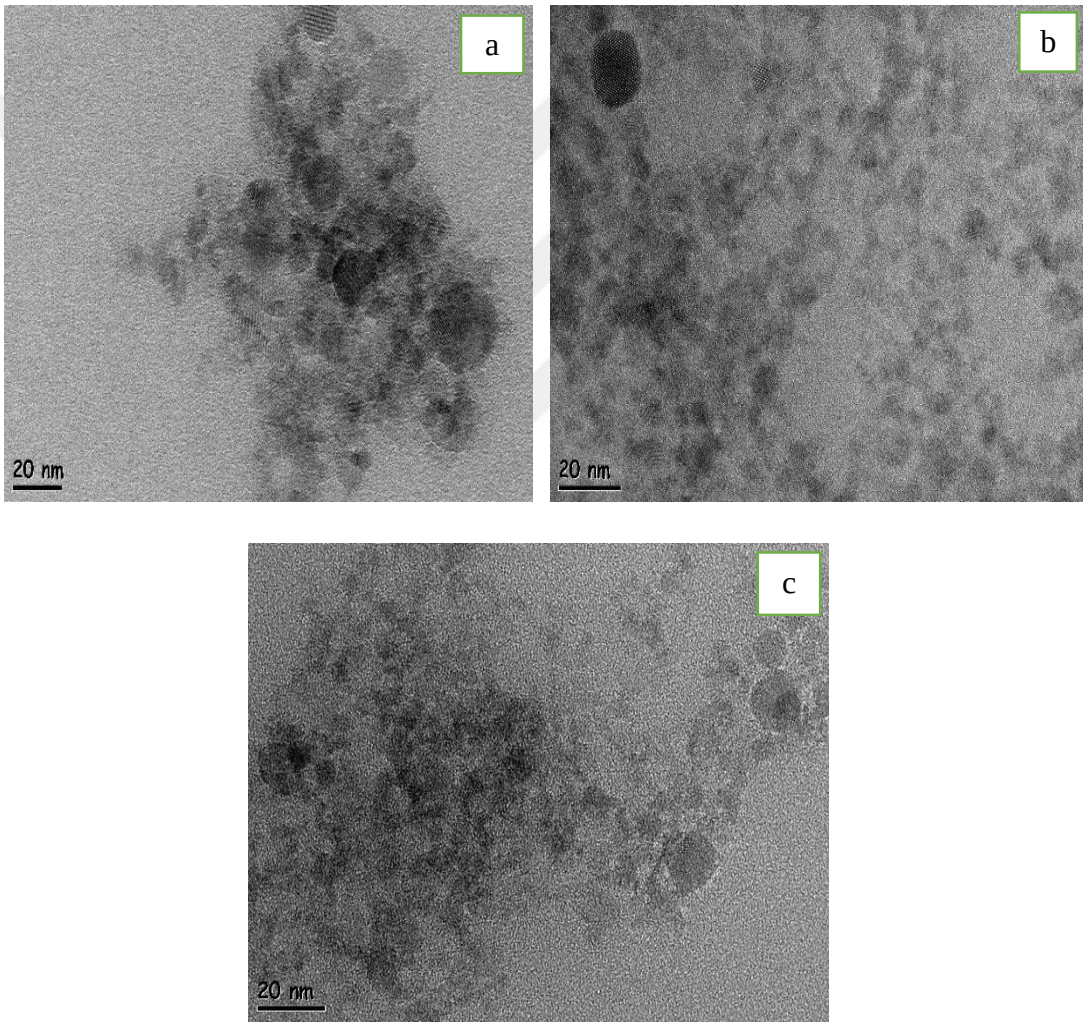

Figure 3.6 TEM images for a) Pure titanium dioxide. b) 5 mole % Cu/TiO_2. c) 10 mole % Cu/TiO_2.

The average nanoparticle sizes have been estimated from 239 spherical particles in the images for the three samples, they are listed in Table 3.7 below. It shows that the product for the three samples have average particle diameter of less than 14 nm.

Table 3.7 TEM average particle sizes.

Sample	d_{TEM}, average (nm)
Pristine TiO_2	8.88
5 mole % Cu/TiO_2	13.78
10 mole % Cu/TiO_2	13.86

Increasing the copper acetate amount from 5 to 10 mole % under the conditions in this work did not make a significant effect on the sizes of nanoparticles for the two samples of doped TiO_2. This is not the case in other studies where they found that increasing copper increased the particles´ sizes [153, 154]. The working conditions like oxygen dispersion, pressure drop, fuel/oxygen ratio, precursor concentrations and flow rate profoundly influence the production of nanoparticles in the FSP process. In this work a pressure drop of 0.3 bar, a fixed amount of GLFR were used. Keeping fixed flow rate for precursor and oxygen dispersion in the three experiments have maintained the height of flame to be the same in all the experiments (the same residence time), but the change in the precursors´ concentrations (by adding copper) has changed the products particle size, crystallinity, anatase-rutile content and specific surface area. The gas to liquid flow ratio (GLFR) of this work is 5000, which is considered as a high value. Table 3.8 below illustrates GLFR ratios used in other works where high oxygen dispersion was used.

Table 3.8 Gas to liquid flow ratio values in some studies where high oxygen dispersion have been used.

GLFR ($lmin^{-1}/l.min^{-1}$)	Reference
2361.6	[155]
2100	[156]
6310	[80]
5000	This work

The effect of GLFR can be seen in increasing the amount of oxygen in the burning region, which intensifies the fuel-oxygen mixing process and decreases the droplet size. The reduced droplet size has a higher surface area that makes it has a fast evaporation rate. The earlier oxidation rate of the fuel mixture is a result of the speedier droplet evaporation rate; this will make the flame height short. Moreover, increasing the flow rate of oxygen dispersion lowers the residence time for the particles in the higher temperature zone of the flames, which would reduce the growth rate for the particle size, making it smaller. The sintering rate depends on flame temperature, velocity, and height. The particles´ growth stops when the temperature comes down, which will make the coagulation rate higher than the sintering rate; this starts to happen when the particles leave the more elevated temperature zone of the flame [155, 156]. The described mechanism for the influence of high oxygen dispersion justifies the small sizes of nanoparticles produced and the particle size distribution in Figure 3.7.

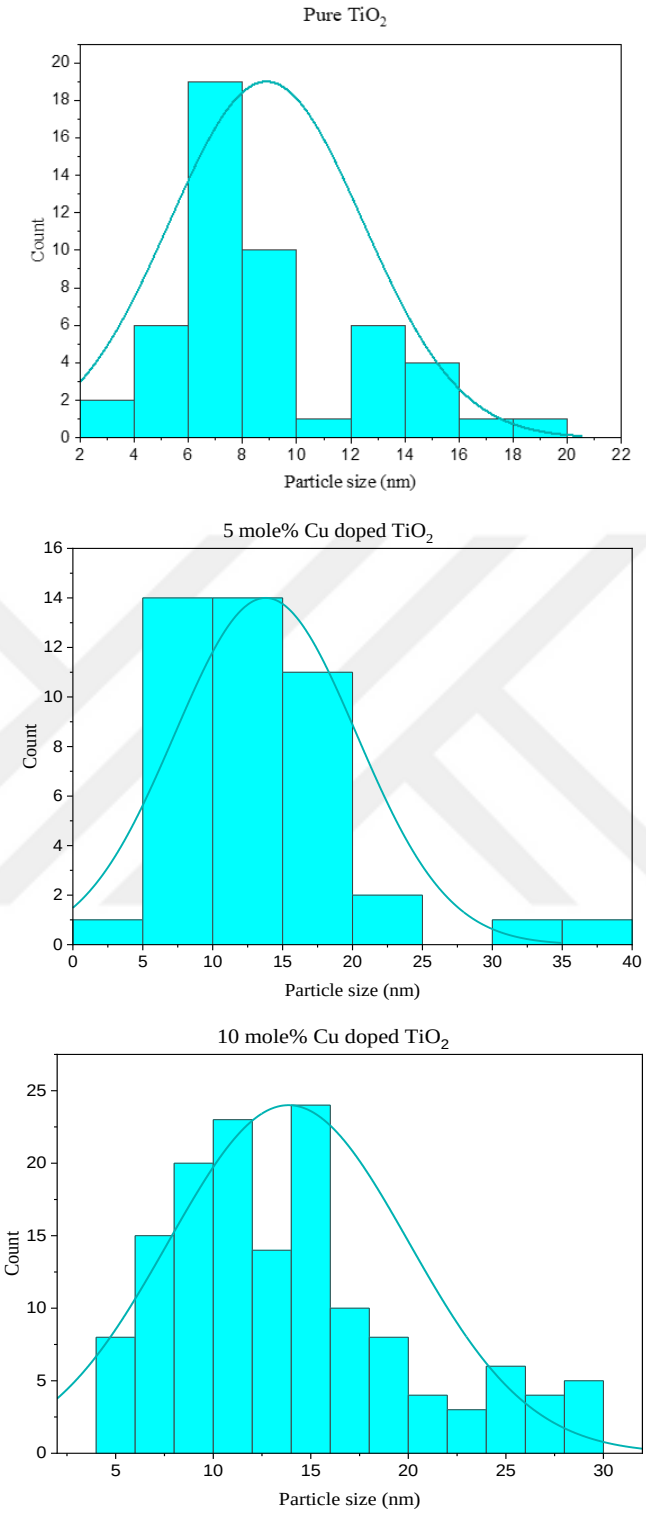

Figure 3.7 Particles size distribution for the manufactured samples.

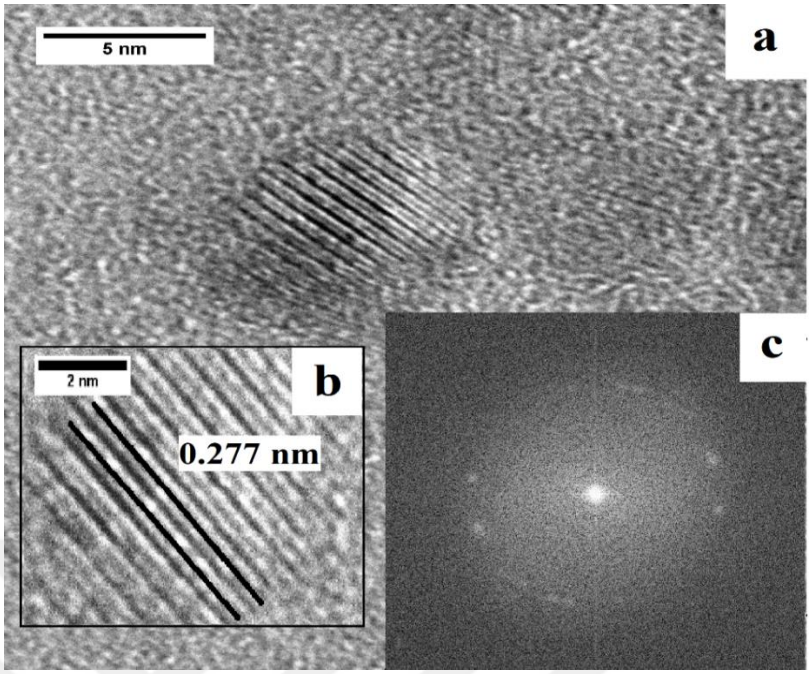

Figure 3.8 a) HRTEM image of pure TiO_2 (scale: 5 nm), b) magnification view of the selected part from image a (scale 2 nm), c) corresponding FFT diffractogram.

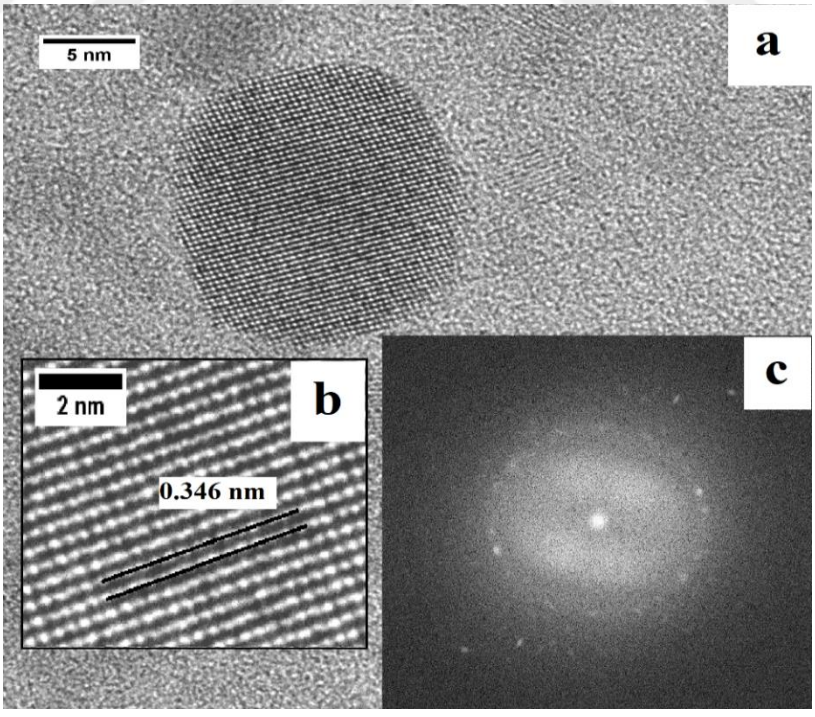

Figure 3.9 a) HRTEM image of 5 mole % Cu/TiO_2 (scale: 5 nm), b) magnification view of the selected part from image a (scale 2 nm), c) corresponding FFT diffractogram.

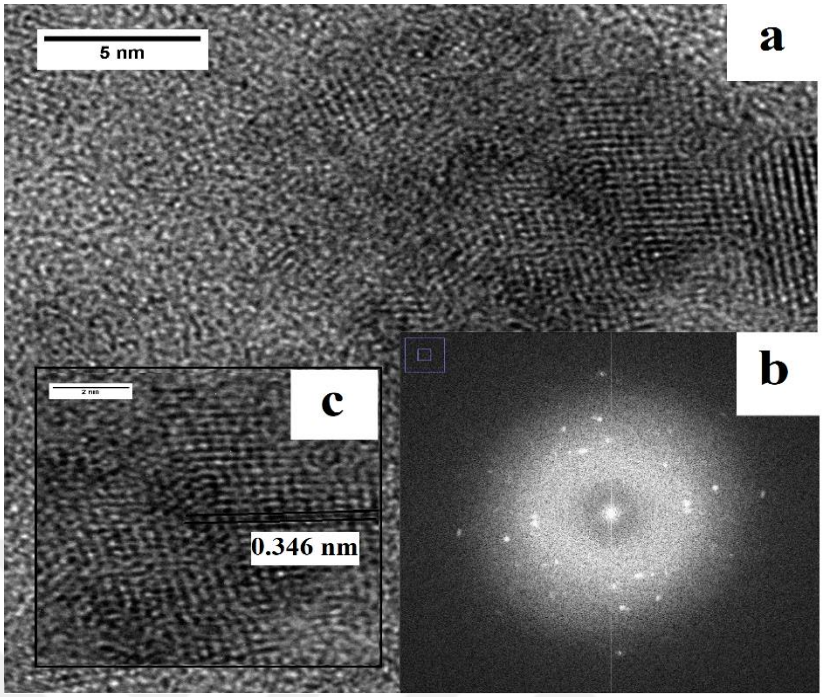

Figure 3.10 a) HRTEM image of 10 mole % Cu/TiO_2 (scale: 5 nm), b) magnification view of the selected part from image a (scale 2 nm), c) corresponding FFT diffractogram.

HRTEM micrographs in Figures 3.8, 3.9 and 3.10 above for the produced nanoparticles using image j program shows images in 2 and 5 nm scale with clear images of their lattice fringes. The lattice spacing 0.277 nm for pure TiO_2 corresponds to (101) crystallographic plane for rutile phase according to Card No.: 00-021-1276, where in XRD analysis results it shows 0.249 nm. For 5 and 10 mole % copper doped titania, both of them show that they have 0.346 lattice spacing corresponding to (101) crystallographic plane, which is in a good agreement with card no 01-075-1537 and card no. 01-086-1157 for anatase, where their values in these cards are 0.347 nm and 0.351 nm, respectively. They are also similar to the XRD d-spacing values for anatase phase, which are 0.352 and 0.352 respectively.

The selected area electron diffraction (SAED) pictures for the three samples are shown in Figure 3.11. They illustrate polycrystalline nature for manufactured materials as they have a clear diffraction rings, but the crystallinity becomes lower in image b and c as the rings become less sharper and the bright spots become less brighter [157].

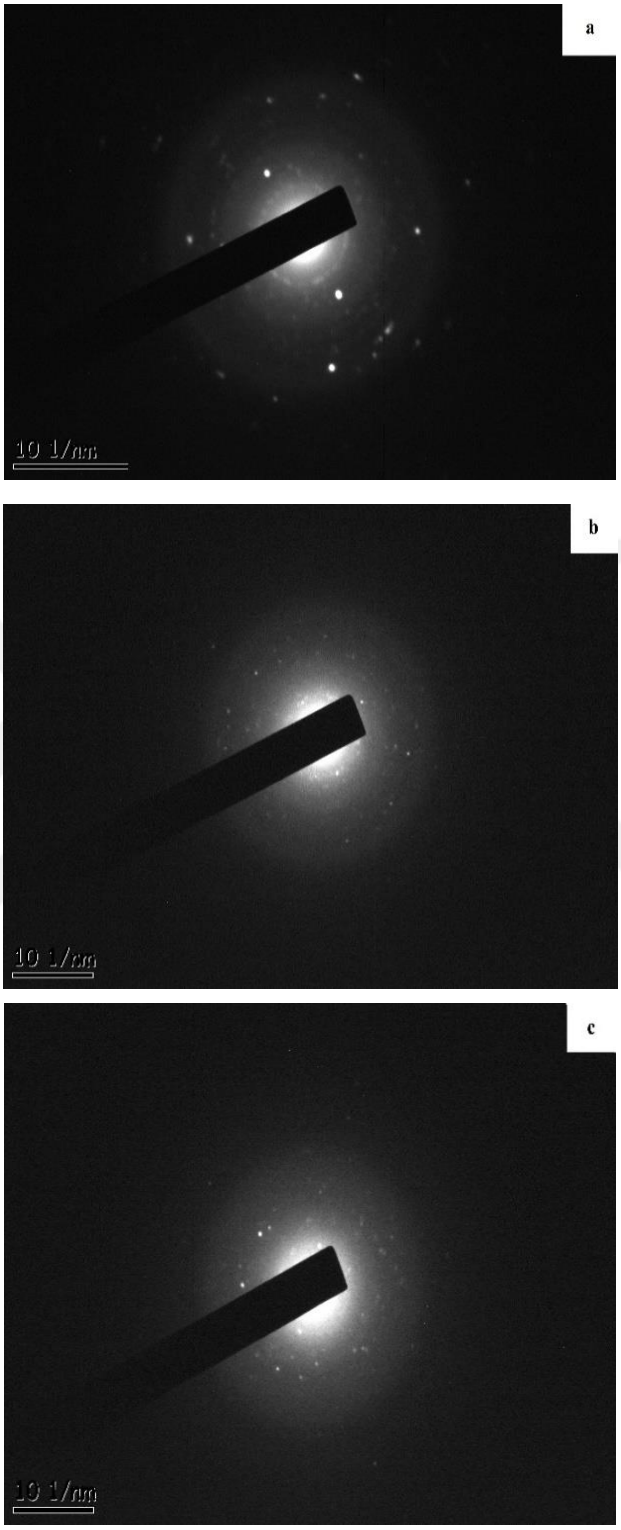

Figure 3.11 SAED diffraction images for a) Pure titanium dioxide, b) 5 mole % Cu/TiO_2, c) 10 mole % Cu/TiO_2.

4.5 UV-vis Diffuse Reflectance Analysis

The band gaps energy values of as-synthesized pure and doped titania were taken from Figure 3.12 below, the curves were drawn depending on the analysis data from the laboratory. The band gaps values taken from Figure 3.12 are listed in Table 3.9.

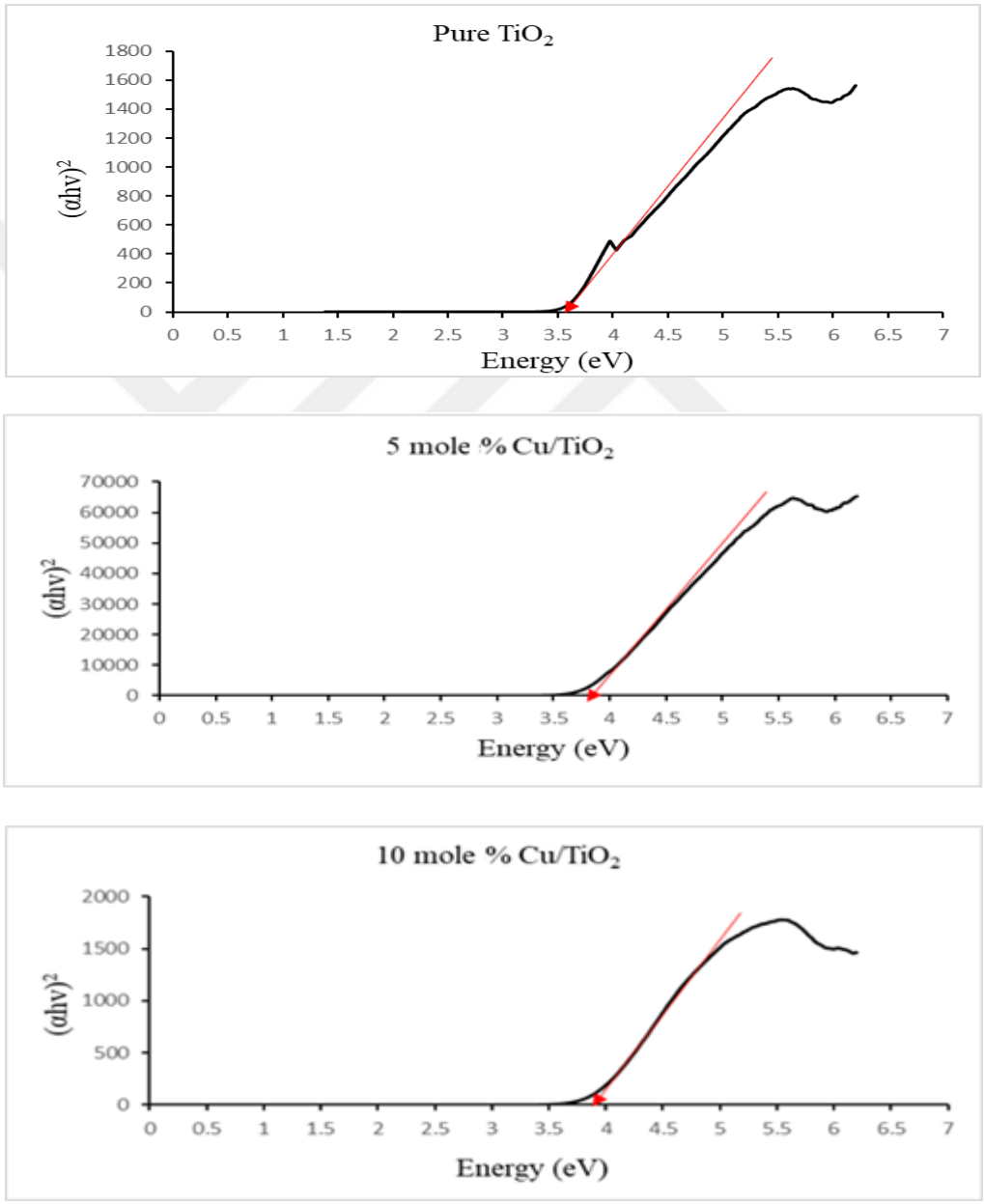

Figure 3.12 Transformed diffuse reflectance spectra (TDRS) for the manufactured powders.

Table 3.9 Band gap values for the manufactured products.

Product	Band gap value (eV)
Pure TiO_2	3.56
5 mole % Cu/TiO_2	3.79
10 mole % Cu/TiO_2	3.85

As Table 3.9 displays, the band gaps of the previously manufactured samples increase with increasing the copper content. In the literature a wide range of Cu doping from 1 to 20 weight percent was used, and they got a red shift in the absorption spectra of their samples [120, 154]. Nevertheless, there are some studies where the band gap energy value of titania increased by doping. Ganesh et al [158] used sol-gel method to prepare copper doped titanium dioxide powders; they note that the band gap of the products enlarge with the addition of more copper. Another study by Munir et al. [159] also used sol-gel method to synthesize TiO_2 and dope it with metals (Cu, Ni, and Cr); they get band gap for pure titanium dioxide of 3.9 eV larger than the normal values (3.0 or 3.2 eV) and a higher band gaps for the other products. They ascribed this effect to the Burstein-Moss effect. According to which, at a specific dopant concentration when the amount of charge carriers is increased, the Fermi level lying in the conduction band is filled. Thereafter the extra excited electrons are presupposed to go in the conduction band (above the Fermi degree). This situation brings about the widening of the band gap of the material, and consequently, a blue shift is noticed in the absorption spectra. In both of the above-mentioned studies, the doped titania was doped using the same quantities of dopants that were narrowed its band gap value in other studies. However, both of Ganesh et al and Munir et al. did not mention the percentages of the amorphous in their samples that may take a role in widening the band gap energy of titanium dioxide, as the amorphous TiO_2 has a wider band gap than crystalline one [160].

CHAPTER 4

4. CONCLUSION AND FUTURE WORK

4.1 Conclusion:

The effect of using high GLFR and low-pressure drop working conditions have been investigated in this work in terms of their effects on the spray conditions and the residence time. The low-pressure drop under the used operating conditions affects the spray properties and producing larger droplets. The larger droplet sizes, coupled with the short residence time means droplets leave the flame without completely evaporating. The escaped, (not complete evaporated), droplets have formed the eggshell structures that are depicted in the SEM pictures.

The results from using the working conditions and copper addition for this work can be seen on their effects on the crystallinity, morphological, structural, and optical properties as well. The crystallinity of the products was decreased until the amorphous contents became the dominating phase in the copper doped samples. The surface area and rutile content were increased also.

Although the purpose of this study was to decrease the band gap of TiO_2 by adding Cu, narrowing in the band gap was not observed. The band gap increased with the addition of copper, which is most likely due to the low residence time, and as a result, less crystallinity.

4.2 Future work:

In light of the XRD characterization results, the next step is to study the operation conditions to increase the residence time in flame to make the products more crystalline, decrease or avoid the formation of the eggshell structures, and narrow the energy band gap. After the completion of this thesis, our research group already started working under conditions with lower GLFR, and increased pressure drop (making it at least 1 bar), and the results showed smaller droplets, and longer residence time for the droplets in the flame, consequently, making the evaporation process more efficient.

The dopant concentration showed a significant effect on increasing the amorphous, rutile content and widening the band gap; it will also be investigated further.

REFERENCES

[1] WWAP and 2017- (Azoulay UNESCO. Director-General A.), "The United Nations world water development report 2019: leaving no one behind." UNESCO.

[2] S. Natarajan, H. C. Bajaj, and R. J. Tayade, "Recent advances based on the synergetic effect of adsorption for removal of dyes from waste water using photocatalytic process," *J. Environ. Sci. (China)*, vol. 65, pp. 201–222, 2018.

[3] Q. Xiang *et al.*, "Interfacial modification of titanium dioxide to enhance photocatalytic efficiency towards H_2 production," *J. Colloid Interface Sci.*, vol. 556, pp. 376–385, Nov. 2019.

[4] A. Madhumitha, V. Preethi, and S. Kanmani, "Photocatalytic hydrogen production using TiO_2 coated iron-oxide core shell particles," *Int. J. Hydrogen Energy*, vol. 43, no. 8, pp. 3946–3956, Feb. 2018.

[5] B. Al-Ghafri, W.-J. Lau, M. Al-Abri, P.-S. Goh, and A. F. Ismail, "Titanium dioxide-modified polyetherimide nanofiber membrane for water treatment," *J. Water Process Eng.*, vol. 32, p. 100970, Dec. 2019.

[6] A. H. Mamaghani, F. Haghighat, and C.-S. Lee, "Photocatalytic degradation of VOCs on various commercial titanium dioxides: Impact of operating parameters on removal efficiency and by-products generation," *Build. Environ.*, vol. 138, pp. 275–282, Jun. 2018.

[7] D. Adekoya, M. Tahir, and N. A. S. Amin, "Recent trends in photocatalytic materials for reduction of carbon dioxide to methanol," *Renew. Sustain. Energy Rev.*, vol. 116, p. 109389, Dec. 2019.

[8] N. Shehzad, M. Tahir, K. Johari, T. Murugesan, and M. Hussain, "Improved interfacial bonding of graphene-TiO_2 with enhanced photocatalytic reduction of CO_2 into solar fuel," *J. Environ. Chem. Eng.*, vol. 6, no. 6, pp. 6947–6957, Dec. 2018.

[9] C. Li *et al.*, “Copper on the inner surface of mesoporous TiO_2 hollow spheres: a highly selective photocatalyst for partial oxidation of methanol to methyl formate,” *Catal. Sci. Technol.*, vol. 9, no. 22, pp. 6240–6252, 2019.

[10] G. F. El Fawal, H. S. Hassan, M. R. El-Aassar, and M. F. Elkady, “Electrospun Polyvinyl Alcohol Nanofibers Containing Titanium Dioxide for Gas Sensor Applications,” *Arab. J. Sci. Eng.*, vol. 44, no. 1, pp. 251–257, 2019.

[11] B. Gökdere, A. Üzer, S. Durmazel, E. Erçağ, and R. Apak, “Titanium dioxide nanoparticles–based colorimetric sensors for determination of hydrogen peroxide and triacetone triperoxide (TATP),” *Talanta*, vol. 202, pp. 402–410, Sep. 2019.

[12] R. D. Chavan, P. Yadav, A. Nimbalkar, S. P. Bhoite, P. N. Bhosale, and C. Kook Hong, “Ruthenium doped mesoporous titanium dioxide for highly efficient, hysteresis-free and stable perovskite solar cells,” *Sol. Energy*, vol. 186, pp. 156–165, Jul. 2019.

[13] P. Selvaraj *et al.*, “Soft-template synthesis of high surface area mesoporous titanium dioxide for dye-sensitized solar cells,” *Int. J. Energy Res.*, vol. 43, no. 1, pp. 523–534, Jan. 2019.

[14] H.-E. Wang *et al.*, “Oxygen-deficient titanium dioxide as a functional host for lithium–sulfur batteries,” *J. Mater. Chem. A*, vol. 7, no. 17, pp. 10346–10353, 2019.

[15] W. Ji *et al.*, “The core-shell mesoporous titanium dioxide with in-situ nitrogen doped carbon as the anode for high performance lithium-ion battery,” *J. Alloys Compd.*, vol. 806, pp. 946–952, Oct. 2019.

[16] H. Torabmostaedi and T. Zhang, “Numerical simulation of TiO_2 nanoparticle synthesis by flame spray pyrolysis,” *Powder Technol.*, vol. 329, pp. 426–433, 2018.

[17] S. Phanichphant, C. Liewhiran, K. Wetchakun, A. Wisitsoraat, and A. Tuantranont, “Flame-made Nb-doped TiO_2 ethanol and acetone sensors,” *Sensors (Basel).*, vol. 11, no. 1, pp. 472–484, 2011.

[18] W. Y. Teoh, R. Amal, L. Mädler, and S. E. Pratsinis, “Flame sprayed visible light-active Fe-TiO_2 for photomineralisation of oxalic acid,” *Catal. Today*, vol. 120, no. 2, pp. 203–213, 2007.

[19] F. Mikaeili, S. Topcu, G. Jodhani, and P. I. Gouma, “Flame-sprayed pure and Ce-doped TiO_2 photocatalysts,” *Catalysts*, vol. 8, no. 9. 2018.

[20] C. Gunawan, W. Y. Teoh, C. P. Marquis, J. Lifia, and R. Amal, “Reversible Antimicrobial Photoswitching in Nanosilver,” *Small*, vol. 5, no. 3, pp. 341–344, Feb. 2009.

[21] A. Teleki, N. Bjelobrk, and S. E. Pratsinis, “Flame-made Nb- and Cu-doped TiO2 sensors for CO and ethanol,” *Sens. Actuators. B. Chem.*, vol. 130, no. 1, pp. 449–457, 2008.

[22] C. Chaisuk, A. Wehatoranawee, S. Preampiyawat, S. Netiphat, A. Shotipruk, and O. Mekasuwandumrong, “Preparation and characterization of CeO_2/TiO_2 nanoparticles by flame spray pyrolysis,” *Ceram. Int.*, vol. 37, no. 5, pp. 1459–1463, 2011.

[23] T. Boningari, S. N. R. Inturi, M. Suidan, and P. G. Smirniotis, “Novel one-step synthesis of sulfur doped-TiO_2 by flame spray pyrolysis for visible light photocatalytic degradation of acetaldehyde,” *Chem. Eng. J.*, vol. 339, pp. 249–258, May 2018.

[24] T. Boningari, S. N. R. Inturi, M. Suidan, and P. G. Smirniotis, “Novel one-step synthesis of nitrogen-doped TiO_2 by flame aerosol technique for visible-light photocatalysis: Effect of synthesis parameters and secondary nitrogen (N) source,” *Chem. Eng. J.*, vol. 350, pp. 324–334, Oct. 2018.

[25] S. N. R. Inturi, T. Boningari, M. Suidan, and P. G. Smirniotis, “Visible-light-induced photodegradation of gas phase acetonitrile using aerosol-made transition metal (V, Cr, Fe, Co, Mn, Mo, Ni, Cu, Y, Ce, and Zr) doped TiO_2,” *Appl. Catal. B Environ.*, vol. 144, pp. 333–342, Jan. 2014.

[26] B. Tian, C. Li, F. Gu, H. Jiang, Y. Hu, and J. Zhang, “Flame sprayed V-doped TiO_2 nanoparticles with enhanced photocatalytic activity under visible light irradiation,” *Chem. Eng. J.*, vol. 151, no. 1, pp. 220–227, 2009.

[27] M. Bernareggi, M. V Dozzi, L. G. Bettini, A. M. Ferretti, G. L. Chiarello, and E. Selli, “Flame-Made Cu/TiO_2 and $Cu-Pt/TiO_2$ Photocatalysts for Hydrogen Production,” *Catalysts* , vol. 7, no. 10. 2017.

[28] I. E. Paulauskas *et al.*, “Photocatalytic activity of doped and undoped titanium dioxide nanoparticles synthesised by flame spray pyrolysis,” *Platin. Met. Rev.*, vol. 57, no. 1, pp. 32–43, 2013.

[29] B. Pongthawornsakun, S. Fujita, M. Arai, O. Mekasuwandumrong, and J. Panpranot, “Mono- and bi-metallic $Au–Pd/TiO_2$ catalysts synthesized by one-step flame spray pyrolysis for liquid-phase hydrogenation of 1-heptyne,” *Appl. Catal. A Gen.*, vol. 467, pp. 132–141, 2013.

[30] L. Meng and H. Zhao, “Low-temperature complete removal of toluene over highly active nanoparticles $CuO-TiO_2$ synthesized via flame spray pyrolysis,” *Appl. Catal. B Environ.*, vol. 264, p. 118427, 2020.

[31] P. YU and M. Cardona, *Fundamentals of Semiconductors: Physics and Materials Properties*. Springer Berlin Heidelberg, 2010.

[32] Advanced Manufacturing Office, “Wide Bandgap Semiconductors : Pursuing the Promise,” *Doe/Ee-0910*, 2013.

[33] M. Alonso and E. J. Finn, *Fundamental university physics. Vol.3: Quantum and statistical physics*. 1968.

[34] C. A. Bignozzi and B. D. Alexander, “Photocatalysis.” Springer, Berlin, 2011.

[35] A. Fujishima, X. Zhang, and D. A. Tryk, “TiO_2 photocatalysis and related surface phenomena,” *Surf. Sci. Rep.*, vol. 63, no. 12, pp. 515–582, 2008.

[36] T. Aditya, A. Pal, and T. Pal, “Nitroarene reduction: a trusted model reaction to test nanoparticle catalysts,” *Chem. Commun.*, vol. 51, no. 46, pp. 9410–9431, 2015.

[37] S. M. Gupta and M. Tripathi, “A review of TiO_2 nanoparticles,” *Chinese Sci. Bull.*, vol. 56, no. 16, pp. 1639–1657, 2011.

[38] S.-Y. Lee and S.-J. Park, “TiO_2 photocatalyst for water treatment applications,” *J. Ind. Eng. Chem.*, vol. 19, no. 6, pp. 1761–1769, 2013.

[39] P. Raizada, A. Sudhaik, and P. Singh, “Photocatalytic water decontamination using graphene and ZnO coupled photocatalysts: A review,” *Mater. Sci. Energy Technol.*, vol. 2, no. 3, pp. 509–525, 2019.

[40] K. A. Adegoke, M. Iqbal, H. Louis, and O. S. Bello, “Synthesis, characterization and application of CdS/ZnO nanorod heterostructure for the photodegradation of Rhodamine B dye,” *Mater. Sci. Energy Technol.*, vol. 2, no. 2, pp. 329–336, 2019.

[41] K. Han, X. L. Peng, F. Li, and M. M. Yao, “SnO2 composite films for enhanced photocatalytic activities,” *Catalysts*, vol. 8, no. 10, pp. 1–12, 2018.

[42] K. Sivula, F. Le Formal, and M. Grätzel, “WO_3–Fe_2O_3 Photoanodes for Water Splitting: A Host Scaffold, Guest Absorber Approach,” *Chem. Mater.*, vol. 21, no. 13, pp. 2862–2867, Jul. 2009.

[43] A. A. Ismail, M. Faisal, and A. Al-Haddad, “Mesoporous WO_3- graphene photocatalyst for photocatalytic degradation of Methylene Blue dye under visible light illumination,” *J. Environ. Sci. (China)*, vol. 66, pp. 328–337, 2018.

[44] V. Etacheri, C. Di Valentin, J. Schneider, D. Bahnemann, and S. C. Pillai, “Visible-light activation of TiO_2 photocatalysts: Advances in theory and experiments,” *J. Photochem. Photobiol. C Photochem. Rev.*, vol. 25, pp. 1–29, 2015.

[45] T. L. Thompson and J. T. Yates, “Surface Science Studies of the Photoactivation of TiO_2 New Photochemical Processes,” *Chem. Rev.*, vol. 106, no. 10, pp. 4428–4453, Oct. 2006.

[46] T. Luttrell, S. Halpegamage, J. Tao, A. Kramer, E. Sutter, and M. Batzill, “Why is anatase a better photocatalyst than rutile? - Model studies on epitaxial TiO_2 films,” *Sci. Rep.*, vol. 4, no. 1, p. 4043, 2014.

[47] S. M. Reda, M. Khairy, and M. A. Mousa, “Photocatalytic activity of nitrogen and copper doped TiO_2 nanoparticles prepared by microwave-assisted sol-gel process,” *Arab. J. Chem.*, vol. 13, no. 1, pp. 86–95, Jan. 2020.

[48] M. Hirano, C. Nakahara, K. Ota, O. Tanaike, and M. Inagaki, “Photoactivity and phase stability of ZrO_2-doped anatase-type TiO_2 directly formed as nanometer-sized particles by hydrolysis under hydrothermal conditions,” *J. Solid State Chem.*, vol. 170, no. 1, pp. 39–47, 2003.

[49] H. Chang and P. J. Huang, “Thermo-Raman studies on anatase and rutile,” *J. Raman Spectrosc.*, vol. 29, no. 2, pp. 97–102, Feb. 1998.

[50] P. Bouras, E. Stathatos, and P. Lianos, “Pure versus metal-ion-doped nanocrystalline titania for photocatalysis,” *Appl. Catal. B Environ.*, vol. 73, no. 1, pp. 51–59, 2007.

[51] A. Sclafani, L. Palmisano, and M. Schiavello, “Influence of the preparation methods of titanium dioxide on the photocatalytic degradation of phenol in aqueous dispersion,” *J. Phys. Chem.*, vol. 94, no. 2, pp. 829–832, Jan. 1990.

[52] B. Tryba, J. Orlikowski, R. J. Wróbel, J. Przepiórski, and A. W. Morawski, “Preparation and Characterization of Rutile-Type TiO_2 Doped with Cu,” *Journal of Materials Engineering and Performance*, vol. 24, no. 3. pp. 1243–1252, 2015.

[53] X. H. Xia, Y. Gao, Z. Wang, and Z. J. Jia, “Structure and photocatalytic properties of copper-doped rutile TiO2 prepared by a low-temperature process,” *J. Phys. Chem. Solids*, vol. 69, no. 11, pp. 2888–2893, Nov. 2008.

[54] H.-S. Chen, C. Su, J.-L. Chen, T.-Y. Yang, N.-M. Hsu, and W.-R. Li, “Preparation and Characterization of Pure Rutile TiO_2 Nanoparticles for Photocatalytic Study and Thin Films for Dye-Sensitized Solar Cells,” *J. Nanomater.*, vol. 2011, p. 869618, 2011.

[55] S. Ahmed, M. G. Rasul, R. Brown, and M. A. Hashib, “Influence of parameters on the heterogeneous photocatalytic degradation of pesticides and phenolic contaminants in wastewater: A short review,” *J. Environ. Manage.*, vol. 92, no. 3, pp. 311–330, 2011.

[56] I. Poulios, M. Kositzi, K. Pitarakis, and S. Beltsios, “Photocatalytic oxidation of methomyl in the presence of semiconducting oxides,” *Int. J. Environ. Pollut.*, vol. 28, no. 1–2, pp. 33–44, Jan. 2006.

[57] R. ENRÍQUEZ and P. PICHAT, “Different Net Effect of TiO_2 Sintering Temperature on the Photocatalytic Removal Rates of 4-Chlorophenol, 4-Chlorobenzoic Acid and Dichloroacetic Acid in Water,” *J. Environ. Sci. Heal. Part A*, vol. 41, no. 6, pp. 955–966, Jul. 2006.

[58] B. F. Abramović, V. N. Despotović, D. V. Šojić, D. Z. Orčić, J. J. Csanádi, and D. D. Četojević-Simin, “Photocatalytic degradation of the herbicide clomazone in natural water using TiO_2: Kinetics, mechanism, and toxicity of degradation products,” *Chemosphere*, vol. 93, no. 1, pp. 166–171, 2013.

[59] A. Moiseev, F. Qi, J. Deubener, and A. Weber, “Photocatalytic activity of nanostructured titanium dioxide from diffusion flame synthesis,” *Chem. Eng. J.*, vol. 170, no. 1, pp. 308–315, May 2011.

[60] A. Carabin, P. Drogui, and D. Robert, “Photo-degradation of carbamazepine using TiO2 suspended photocatalysts,” *J. Taiwan Inst. Chem. Eng.*, vol. 54, pp. 109–117, Sep. 2015.

[61] H. K. Singh, M. Saquib, M. M. Haque, and M. Muneer, “Heterogeneous photocatalysed degradation of 4-chlorophenoxyacetic acid in aqueous suspensions,” *J. Hazard. Mater.*, vol. 142, no. 1, pp. 374–380, 2007.

[62] B. Zielińska, J. Grzechulska, R. J. Kaleńczuk, and A. W. Morawski, “The pH influence on photocatalytic decomposition of organic dyes over A11 and P25 titanium dioxide,” *Appl. Catal. B Environ.*, vol. 45, no. 4, pp. 293–300, Oct. 2003.

[63] H. Li *et al.*, “Mesoporous Titania Spheres with Tunable Chamber Stucture and Enhanced Photocatalytic Activity,” *J. Am. Chem. Soc.*, vol. 129, no. 27, pp. 8406–8407, Jul. 2007.

[64] A. A. Altaf, M. Ahmed, M. Hamayun, S. Kausar, M. Waqar, and A. Badshah, “Titania nano-fibers: A review on synthesis and utilities,” *Inorganica Chim. Acta*, vol. 501, p. 119268, Feb. 2020.

[65] S. Khanna *et al.*, “Growth of titanium dioxide nanorod over shape memory material using chemical vapor deposition for energy conversion application,” *Mater. Today Proc.*, Dec. 2019.

[66] Y. Cui *et al.*, “Fabrication of bismuth oxide/titanium dioxide nano-tube arrays photoelectrode and its enhanced visible light photocatalytic performance for degradation of 4-chlorphenol,” *Electrochim. Acta*, vol. 246, pp. 1075–1081, Aug. 2017.

[67] Z. Barbieriková *et al.*, “N-Doped titanium dioxide nanosheets: Preparation, characterization and UV/visible-light activity,” *Appl. Catal. B Environ.*, vol. 232, pp. 397–408, Sep. 2018.

[68] G. Hasegawa, K. Morisato, K. Kanamori, and K. Nakanishi, “New hierarchically porous titania monoliths for chromatographic separation media,” *J. Sep. Sci.*, vol. 34, no. 21, pp. 3004–3010, Nov. 2011.

[69] C. Negi, H. Sharma, P. Kandwal, R. Singhal, and C. Dwivedi, “Carbon-doped titanium dioxide nanoparticles: A facile synthesis, characterization and their photocatalytic activity,” *Mater. Today Proc.*, Jan. 2020.

[70] Z. Sarteep, A. E. Pirbazari, and M. A. Aroon, “Silver Doped TiO_2 Nanoparticles: Preparation, Characterization and Efficient Degradation of 2,4-dichlorophenol Under Visible Light,” *Nanotechnol. J. Water Environ. Nanotechnol*, vol. 1, no. 12. 2016.

[71] L. G. Bettini, M. V. Diamanti, M. Sansotera, M. P. Pedeferri, W. Navarrini, and P. Milani, "Immobilized TiO_2 nanoparticles produced by flame spray for photocatalytic water remediation," *Journal of Nanoparticle Research*, vol. 18, no. 8. 2016.

[72] H. D. Jang, S. K. Kim, and S. J. Kim, "Effect of particle size and phase composition of titanium dioxide nanoparticles on the photocatalytic properties," *Journal of Nanoparticle Research*, vol. 3, no. 2–3. pp. 141–147, 2001.

[73] W. Li and T. Zeng, "Preparation of TiO2 Anatase Nanocrystals by $TiCl_4$ Hydrolysis with Additive H_2SO_4," *PLoS One*, vol. 6, no. 6, pp. 1–6, 2011.

[74] T. Morikawa, T. Ohwaki, K. ichi Suzuki, S. Moribe, and S. Tero-Kubota, "Visible-light-induced photocatalytic oxidation of carboxylic acids and aldehydes over N-doped TiO_2 loaded with Fe, Cu or Pt," *Applied Catalysis B: Environmental*, vol. 83, no. 1–2. pp. 56–62, 2008.

[75] Z. Zhai, K. Zou, W. Feng, and Q. Wang, "Experimental Study on Nitrogen-Doped Nano-Scale TiO2 Prepared by Microwave-Assisted Process at Low Temperature," *Modern Applied Science*, vol. 4, no. 2. 2010.

[76] C. T. Nam, W.-D. Yang, and L. M. Duc, "Solvothermal Synthesis of TiO_2 Photocatalysts in Ketone Solvents with Low Boiling Points," *J. Nanomater.*, vol. 2013, p. 627385, 2013.

[77] W. Y. Teoh, R. Amal, and L. Mädler, "Flame spray pyrolysis: An enabling technology for nanoparticles design and fabrication," *Nanoscale*, vol. 2, no. 8, pp. 1324–1347, 2010.

[78] R. Koirala, S. E. Pratsinis, and A. Baiker, "Synthesis of catalytic materials in flames: opportunities and challenges," *Chem. Soc. Rev.*, vol. 45, no. 11, pp. 3053–3068, 2016.

[79] E. Grades and D. P. Kilian, “Flame Spray Synthesis of Semiconducting Oxide Nanomaterials Fundamental Process Characterization and Control of Product Properties Flammenspray-Synthese halbleitender oxidischer Nanomaterialien Grundlegende Prozesscharakterisierung und Einstellung von Pro,” der Universität Erlangen-Nürnberg zur Erlangung des Grades, 2016.

[80] L. Mädler, H. K. Kammler, R. Mueller, and S. E. Pratsinis, “Controlled synthesis of nanostructured particles by flame spray pyrolysis,” *J. Aerosol Sci.*, vol. 33, no. 2, pp. 369–389, Feb. 2002.

[81] R. Mueller, L. Mädler, and S. E. Pratsinis, “Nanoparticle synthesis at high production rates by flame spray pyrolysis,” *Chem. Eng. Sci.*, vol. 58, no. 10, pp. 1969–1976, 2003.

[82] Y. Wang, Q. Wang, X. Zhan, F. Wang, M. Safdar, and J. He, “Visible light driven type II heterostructures and their enhanced photocatalysis properties: a review,” *Nanoscale*, vol. 5, no. 18, pp. 8326–8339, 2013.

[83] A. Maurya and P. Chauhan, “Structural and optical characterization of CdS/TiO_2 nanocomposite,” *Mater. Charact.*, vol. 62, no. 4, pp. 382–390, Apr. 2011.

[84] T. Chen and B. Liu, “Enhanced dielectric performance of poly(vinylidene fluoride) composite filled with copper phthalocyanine-titanium dioxide ball milling hybrids,” *Mater. Lett.*, vol. 209, pp. 467–471, 2017.

[85] M. H. Farzana and S. Meenakshi, “Exploitation of zinc oxide impregnated chitosan beads for the photocatalytic decolorization of an azo dye,” *Int. J. Biol. Macromol.*, vol. 72, pp. 900–910, Jan. 2015.

[86] M. Ni, M. K. H. Leung, D. Y. C. Leung, and K. Sumathy, “A review and recent developments in photocatalytic water-splitting using TiO_2 for hydrogen production,” *Renew. Sustain. Energy Rev.*, vol. 11, no. 3, pp. 401–425, 2007.

[87] and C. H. S. C. C. H. Ashok, V. K. Rao, “CuO/TiO_2 Metal Oxide Nanocomposite Synthesis via Room Temperature Ionic Liquid,” *J. Nanomater. Mol. Nanotechnol.*, vol. 05, no. 02, 2016.

[88] M. Hasmath Farzana and S. Meenakshi, “Photocatalytic aptitude of titanium dioxide impregnated chitosan beads for the reduction of Cr(VI),” *Int. J. Biol. Macromol.*, vol. 72, pp. 1265–1271, 2015.

[89] O. Ola and M. M. Maroto-Valer, “Review of material design and reactor engineering on TiO2 photocatalysis for CO_2 reduction,” *J. Photochem. Photobiol. C Photochem. Rev.*, vol. 24, pp. 16–42, Sep. 2015.

[90] K. Al-Attafi, A. Nattestad, S. X. Dou, and J. H. Kim, “A Comparative Study of TiO_2 Paste Preparation Methods Using Solvothermally Synthesised Anatase Nanoparticles in Dye-Sensitised Solar Cells,” *Appl. Sci.*, vol. 9, no. 5, 2019.

[91] H. Lai, X. Liu, F. Zeng, G. Peng, J. Li, and Z. Yi, “Multicarbazole-Based D−π–A Dyes Sensitized Hydrogen Evolution under Visible Light Irradiation,” *ACS Omega*, vol. 5, no. 4, pp. 2027–2033, Feb. 2020.

[92] T. Wang, M. Xia, and X. Kong, “The Pros and Cons of Polydopamine-Sensitized Titanium Oxide for the Photoreduction of CO2,” *Catalysts*, vol. 8, no. 5, 2018.

[93] K. Sharma, V. Sharma, and S. S. Sharma, “Dye-Sensitized Solar Cells: Fundamentals and Current Status,” *Nanoscale Res. Lett.*, vol. 13, no. 1, p. 381, 2018.

[94] J. Li, Y. E, L. Lian, and W. Ma, “Visible light induced dye-sensitized photocatalytic hydrogen production over platinized TiO_2 derived from decomposition of platinum complex precursor,” *Int. J. Hydrogen Energy*, vol. 38, no. 25, pp. 10746–10753, Aug. 2013.

[95] X. CHEN, “Titanium Dioxide Nanomaterials and Their Energy Applications,” *Chinese J. Catal.*, vol. 30, no. 8, pp. 839–851, Aug. 2009.

[96] C. Wang, R. L. Thompson, J. Baltrus, and C. Matranga, “Visible Light Photoreduction of CO_2 Using CdSe/Pt/TiO_2 Heterostructured Catalysts,” *J. Phys. Chem. Lett.*, vol. 1, no. 1, pp. 48–53, Jan. 2010.

[97] T. Wu, T. Lin, J. Zhao, H. Hidaka, and N. Serpone, "TiO_2-Assisted Photodegradation of Dyes. 9. Photooxidation of a Squarylium Cyanine Dye in Aqueous Dispersions under Visible Light Irradiation," *Environ. Sci. Technol.*, vol. 33, no. 9, pp. 1379–1387, May 1999.

[98] O. Carp, C. L. Huisman, and A. Reller, "Photoinduced reactivity of titanium dioxide," *Prog. Solid State Chem.*, vol. 32, no. 1–2, pp. 33–177, 2004.

[99] F. Amano, M. Nakata, J. J. M. Vequizo, and A. Yamakata, "Enhanced Visible Light Response of TiO_2 Codoped with Cr and Ta Photocatalysts by Electron Doping," *ACS Appl. Energy Mater.*, vol. 2, no. 5, pp. 3274–3282, May 2019.

[100] Z. Wang, H. Chen, W. Nian, J. Fan, Y. Li, and X. Wang, "Bismuth oxide modified europium and niobium co-doped titanium dioxide ceramics: Colossal permittivity and low dielectric loss design," *J. Alloys Compd.*, vol. 777, pp. 317–324, 2019.

[101] K. Chiang, R. Amal, and T. Tran, "Photocatalytic degradation of cyanide using titanium dioxide modified with copper oxide," *Adv. Environ. Res.*, vol. 6, no. 4, pp. 471–485, 2002.

[102] S. Ahadi, N. S. Moalej, and S. Sheibani, "Characteristics and photocatalytic behavior of Fe and Cu doped TiO_2 prepared by combined sol-gel and mechanical alloying," *Solid State Sci.*, vol. 96, p. 105975, 2019.

[103] M. F. Ashby *et al.*, *Engineering Materials and Processes Desk Reference*. Elsevier Science & Technology Books, 2008.

[104] R. Janes, L. J. Knightley, and C. J. Harding, "Structural and spectroscopic studies of iron (III) doped titania powders prepared by sol-gel synthesis and hydrothermal processing," *Dye. Pigment.*, vol. 62, no. 3, pp. 199–212, 2004.

[105] E. G. Seebauer and M. C. Kratzer, *Charged semiconductor defects: structure, thermodynamics and diffusion*. Springer Science & Business Media, 2008.

[106] D. J. Reidy, J. D. Holmes, and M. A. Morris, “The critical size mechanism for the anatase to rutile transformation in TiO2 and doped-TiO_2,” *J. Eur. Ceram. Soc.*, vol. 26, no. 9, pp. 1527–1534, 2006.

[107] L. Sun, J. Li, C. L. Wang, S. F. Li, H. B. Chen, and C. J. Lin, “An electrochemical strategy of doping Fe^{3+} into TiO_2 nanotube array films for enhancement in photocatalytic activity,” *Sol. Energy Mater. Sol. Cells*, vol. 93, no. 10, pp. 1875–1880, Oct. 2009.

[108] C. M. Teh and A. R. Mohamed, “Roles of titanium dioxide and ion-doped titanium dioxide on photocatalytic degradation of organic pollutants (phenolic compounds and dyes) in aqueous solutions: A review,” *J. Alloys Compd.*, vol. 509, no. 5, pp. 1648–1660, 2011.

[109] Z. Zhang, C.-C. Wang, R. Zakaria, and J. Y. Ying, “Role of Particle Size in Nanocrystalline TiO_2- Based Photocatalysts,” *J. Phys. Chem. B*, vol. 102, no. 52, pp. 10871–10878, Dec. 1998.

[110] Z. Zafar, I. Ali, S. Park, and J.-O. Kim, “Effect of different iron precursors on the synthesis and photocatalytic activity of Fe–TiO_2 nanotubes under visible light,” *Ceram. Int.*, vol. 46, no. 3, pp. 3353–3366, Feb. 2020.

[111] A. Makdee, P. Unwiset, K. C. Chanapattharapol, and P. Kidkhunthod, “Effects of Ce addition on the properties and photocatalytic activity of TiO_2, investigated by X-ray absorption spectroscopy,” *Mater. Chem. Phys.*, vol. 213, pp. 431–443, 2018.

[112] D. A. H. Hanaor and C. C. Sorrell, “Review of the anatase to rutile phase transformation,” *J. Mater. Sci.*, vol. 46, no. 4, pp. 855–874, 2011.

[113] S. B. Patil, P. S. Basavarajappa, N. Ganganagappa, M. S. Jyothi, A. V. Raghu, and K. R. Reddy, “Recent advances in non-metals-doped TiO_2 nanostructured photocatalysts for visible-light driven hydrogen production, CO_2 reduction and air purification,” *Int. J. Hydrogen Energy*, vol. 44, no. 26, pp. 13022–13039, May 2019.

[114] P. S. Basavarajappa, S. B. Patil, N. Ganganagappa, K. R. Reddy, A. V. Raghu, and C. V. Reddy, "Recent progress in metal-doped TiO_2, non-metal doped/codoped TiO_2 and TiO_2 nanostructured hybrids for enhanced photocatalysis," *Int. J. Hydrogen Energy*, Aug. 2019.

[115] A. Valero Delgado, "2 - Mineral resource depletion assessment," F. Pacheco-Torgal, L. F. Cabeza, J. Labrincha, and A. B. T.-E. C. and B. M. de Magalhães, Eds. Woodhead Publishing, 2014, pp. 13–37.

[116] J. Dai, Z. Suo, Z. Li, and S. Gao, "Effect of Cu/Al doping on electronic structure and optical properties of ZnO," *Results Phys.*, vol. 15, p. 102649, 2019.

[117] S. Zhu *et al.*, "Synthesis of Cu-doped WO_3 materials with photonic structures for high performance sensors," *J. Mater. Chem.*, vol. 20, pp. 9126–9132, Oct. 2010.

[118] S. Tada, K. Fujiwara, T. Yamamura, M. Nishijima, S. Uchida, and R. Kikuchi, "Flame spray pyrolysis makes highly loaded Cu nanoparticles on ZrO_2 for CO_2 to methanol hydrogenation," *Chem. Eng. J.*, vol. 381, p. 122750, 2020.

[119] G. K. Mor *et al.*, "p-Type Cu−Ti−O Nanotube Arrays and Their Use in Self-Biased Heterojunction Photoelectrochemical Diodes for Hydrogen Generation," *Nano Lett.*, vol. 8, no. 10, p. 3555, Oct. 2008.

[120] M. Sahu and P. Biswas, "Single-step processing of copper-doped titania nanomaterials in a flame aerosol reactor," *Nanoscale Res. Lett.*, vol. 6, no. 1, p. 441, 2011.

[121] C.-Y. Tsai, H.-C. Hsi, T.-H. Kuo, Y.-M. Chang, and J.-H. Liou, "Preparation of Cu-Doped TiO2 Photocatalyst with Thermal Plasma Torch for Low-Concentration Mercury Removal," *Aerosol Air Qual. Res.*, vol. 13, pp. 639–648, Apr. 2013.

[122] Chung, F. H., Smith, and D. K., *Industrial Applications of X-ray Diffraction*. 2000.

[123] M. Lee, *X-Ray Diffraction for Materials Research*. New York: Apple Academic Press, 2016.

[124] Y. Waseda, E. Matsubara, and K. Shinoda, *X-ray diffraction crystallography: introduction, examples and solved problems*. Springer Science & Business Media, 2011.

[125] R. Gilles, D. Mukherji, M. Hoelzel, P. Strunz, D. M. Toebbens, and B. Barbier, "Neutron and X-ray diffraction measurements on micro- and nano-sized precipitates embedded in a Ni-based superalloy and after their extraction from the alloy," *Acta Mater.*, vol. 54, no. 5, pp. 1307–1316, 2006.

[126] R. A. Spurr and H. Myers, "Quantitative Analysis of Anatase-Rutile Mixtures with an X-Ray Diffractometer," *Anal. Chem.*, vol. 29, no. 5, pp. 760–762, May 1957.

[127] K. S. W. Sing *et al.*, "Reporting Physisorption Data for Gas/Solid Systems," *Handbook of Heterogeneous Catalysis*. pp. 1217–1230, 15-Mar-2008.

[128] J. Rouquerol, F. Rouquerol, P. Llewellyn, G. Maurin, and K. S. W. Sing, *Adsorption by powders and porous solids: principles, methodology and applications*. Academic press, 2013.

[129] B. J. F. D. Savile Bradbury, "Scanning electron microscope," *Encyclopedia Britannica Online*. Encyclopædia Britannica, inc.

[130] A. Mohammed and A. Abdullah, *Scanning Electron Microscopy (SEM): A Review*. 2019.

[131] C. Escalante and E. Sierra, "Fundamentals of transmission electron microscopy, the technique with the best resolution in the world," Feb. 2019.

[132] B. M. Weckhuysen, "Ultraviolet-visible spectroscopy," 2004.

[133] F. C. B. T.-A. in C. Jentoft, "Chapter 3 Ultraviolet–Visible–Near Infrared Spectroscopy in Catalysis: Theory, Experiment, Analysis, and Application Under Reaction Conditions," vol. 52, Academic Press, 2009, pp. 129–211.

[134] J. Tauc, R. Grigorovici, and A. Vancu, “Optical Properties and Electronic Structure of Amorphous Germanium,” *Phys. status solidi*, vol. 15, no. 2, pp. 627–637, Jan. 1966.

[135] O. Schevciw and W. B. White, “The optical absorption edge of rare earth sesquisulfides and alkaline earth - rare earth sulfides,” *Mater. Res. Bull.*, vol. 18, no. 9, pp. 1059–1068, 1983.

[136] E. Peter Etape, L. John Ngolui, J. Foba-Tendo, D. M. Yufanyi, and B. Victorine Namondo, “Synthesis and Characterization of CuO, TiO_2, and CuO-TiO_2 Mixed Oxide by a Modified Oxalate Route,” *J. Appl. Chem.*, vol. 2017, p. 4518654, 2017.

[137] B. D. C. and S. R. Stock, *Elements of X-ray Diffraction, Third Edition*. Prentice-Hall, 2001.

[138] Y. Wang, W. Duan, B. Liu, X. Chen, F. Yang, and J. Guo, “The Effects of Doping Copper and Mesoporous Structure on Photocatalytic Properties of TiO_2,” *J. Nanomater.*, vol. 2014, p. 178152, 2014.

[139] M. S. P. Francisco and V. R. Mastelaro, “Inhibition of the Anatase−Rutile Phase Transformation with Addition of CeO_2 to CuO−TiO_2 System: Raman Spectroscopy, X-ray Diffraction, and Textural Studies,” *Chem. Mater.*, vol. 14, no. 6, pp. 2514–2518, Jun. 2002.

[140] P. Unwiset, A. Makdee, K. C. Chanapattharapol, and P. Kidkhunthod, “Effect of Cu addition on TiO_2 surface properties and photocatalytic performance: X-ray Absorption Spectroscopy analysis,” *J. Phys. Chem. Solids*, vol. 120, pp. 231–240, 2018.

[141] M. I. Ahmad, S. S. Bhattacharya, C. Fasel, and H. Hahn, “Effect of gas flow rates on the anatase-rutile transformation temperature of nanocrystalline TiO_2 synthesised by chemical vapour synthesis.,” *J. Nanosci. Nanotechnol.*, vol. 9, no. 9, pp. 5572–5577, Sep. 2009.

[142] G. Leofanti, M. Padovan, G. Tozzola, and B. Venturelli, “Surface area and pore texture of catalysts,” *Catal. Today*, vol. 41, no. 1, pp. 207–219, 1998.

[143] K. Alamelu, V. Raja, L. Shiamala, and B. M. Jaffar Ali, "Biphasic TiO_2 nanoparticles decorated graphene nanosheets for visible light driven photocatalytic degradation of organic dyes," *Appl. Surf. Sci.*, vol. 430, pp. 145–154, 2018.

[144] H. Widiyandari, A. Purwanto, V. Gunawan, and S. Widyanto, "Synthesis of Titanium Dioxide (TiO_2) Fine particle by Flame Spray Pyrolysis (FSP) Method using Liquid Petroleum Gas (LPG) as Fuel," *Reaktor*, vol. 17, p. 226, Feb. 2018.

[145] J. Condon, *Surface Area and Porosity Determinations by Physisorption: Measurements and Theory*. 2006.

[146] S. Mavengere, S.-C. Jung, and J.-S. Kim, "Visible light photocatalytic activity of $NaYF_4$:(Yb,Er)-CuO/TiO_2 composite," *Catalysts*, vol. 8, p. 521, Nov. 2018.

[147] S. M. Seyed-Talebi, I. Kazeminezhad, and H. Motamedi, "TiO2 hollow spheres as a novel antibiotic carrier for the direct delivery of gentamicin," *Ceram. Int.*, vol. 44, no. 12, pp. 13457–13462, 2018.

[148] L. Qi, X. Tang, Z. Wang, and X. Peng, "Pore characterization of different types of coal from coal and gas outburst disaster sites using low temperature nitrogen adsorption approach," *Int. J. Min. Sci. Technol.*, vol. 27, no. 2, pp. 371–377, 2017.

[149] S. Venkateswarlu and M. Yoon, "Rapid removal of cadmium ions using green-synthesized Fe_3O_4 nanoparticles capped with diethyl- 4- (4 amino-5-mercapto-4H-1, 2, 4-triazol-3-yl)phenyl phosphonate," *RSC Adv.*, vol. 5, no. 80, pp. 65444–65453, 2015.

[150] T. Yuan *et al.*, "N-doped pierced graphene microparticles as a highly active electrocatalyst for Li-air batteries," *2D Mater.*, vol. 2, no. 2, p. 24002, Apr. 2015.

[151] A. M. Silvestre-Albero, J. M. Juárez-Galán, J. Silvestre-Albero, and F. Rodríguez-Reinoso, "Low-Pressure Hysteresis in Adsorption: An Artifact?," *J. Phys. Chem. C*, vol. 116, no. 31, pp. 16652–16655, Aug. 2012.

[152] K. S. W. Sing, “Reporting physisorption data for gas/solid systems with special reference to the determination of surface area and porosity (Recommendations 1984),” *Pure Appl. Chem.*, vol. 57, no. 4, pp. 603–619, 1985.

[153] Slamet, H. W. Nasution, E. Purnama, S. Kosela, and J. Gunlazuardi, “Photocatalytic reduction of CO2 on copper-doped Titania catalysts prepared by improved-impregnation method,” *Catal. Commun.*, vol. 6, no. 5, pp. 313–319, 2005.

[154] X. Chen, Z. Xu, F. Yang, and H. Zhao, “Flame spray pyrolysis synthesized CuO-TiO 2 nanoparticles for catalytic combustion of lean CO,” *Proc. Combust. Inst.*, 2019.

[155] H. Torabmostaedi and T. Zhang, “Effect of nozzle geometry and processing parameters on the formation of nanoparticles using FSP,” *Chem. Eng. Res. Des.*, vol. 92, no. 11, pp. 2470–2478, 2014.

[156] H. Torabmostaedi and T. Zhang, “Computational study of the effect of processing parameters on the formation and growth of ZrO_2 nanoparticles in FSP process,” *Chem. Eng. Process. Process Intensif.*, vol. 78, pp. 1–10, 2014.

[157] D. B. Williams and C. B. Carter, *Transmission Electron Microscopy: A Textbook for Materials Science*, no. v. 1. Springer, 2009.

[158] I. Ganesh *et al.*, “Preparation and characterization of Cu-doped TiO_2 materials for electrochemical, photoelectrochemical, and photocatalytic applications,” *Appl. Surf. Sci.*, vol. 293, pp. 229–247, 2014.

[159] S. Munir, S. M. Shah, H. Hussain, and R. Ali khan, “Effect of carrier concentration on the optical band gap of TiO_2 nanoparticles,” *Mater. Des.*, vol. 92, pp. 64–72, 2016.

[160] V. I. B. R. A. T. N. A. L. Spectroscopies *et al.*, “Titanium Dioxide Versatile Solid Crystalline: An Overview,” in *Intech*, vol. i, no. tourism, 2016, p. 13.